Design principles of plant root morphogenesis

Marco Marconi[1], Marçal Gallemi[2], Eva Benková[2], Krzysztof Wabnik[1*]

[1]Centro de Biotecnología y Genómica de Plantas, Universidad Politécnica de Madrid (UPM)—Instituto Nacional de Investigación y Tecnología Agraria y Alimentaria (INIA), Pozuelo de Alarcón (Madrid), Spain

[2]Institute of Science and Technology (IST) Austria, 3400 Klosterneuburg, Austria.

[*] Email for correspondence: k.wabnik@upm.es

Manuscript includes:

Main Text
Figures 1 to 6
Supplementary Figs. S1-S9
Supplementary Movie S1-S12 legends
Supplementary Information

Abstract

Understanding how an independent organ develops from the stem cell populations in the process called morphogenesis is a pressing challenge in developmental biology and medicine. Plants build up new organs such as roots to adjust their bodies to dynamic changes in the environment, thereby providing a tractable model to address this challenge. Here, we combined empirical data with advanced computer modeling techniques to build a mechanistic cell-based framework for the morphogenesis of the plant root. Our framework relies on experimentally supported design principles underlying the multi-layered feedback between tissue mechanics, cell growth, and directional cell-to-cell transport of growth regulator auxin. Model simulations reconstruct experimentally-observed patterns of anisotropic growth, auxin distribution, and cell polarity, as well as several root phenotypes caused by chemical, mechanical, or genetic perturbations. Furthermore, our model provides new insights into mechanisms of sustained root growth and cell polarity establishment. This work reveals that mobile auxin signal feeds back on cell polarity and growth mechanics to instruct the morphogenesis of an independent organ.

Introduction

Self-organization is a fundamental attribute of life that is present at multiple scales, from complex ecosystems to individual atoms in proteins. In that sense, plants are remarkable self-organizers as they can successively produce new organs from small stem cell populations, thereby adapting to the dynamically changing environment. Despite the lack of a central nervous system, organs such as roots can coordinate growth through local interactions between adjacent non-mobile cells to sustain the optimal exploration of soil-derived resources[1,2], and provide water and mineral absorption as well as the stable anchor on the ground[3].

Roots grow anisotropically following asymmetric (polar) patterns of cell proliferation and cell expansion[4]. Since plants lack animal polarity components, alternative signalling routes might exist, directly contributing to the onset of plant cell polarity[5–7]. Several plant cell polarity markers have been identified to date, including PIN-FORMED (PIN) transporters of plant hormone auxin[8], plant-specific Rho-GTPases[9] as well as regulators of cell division orientation BASL(Breaking of Asymmetry in the Stomata Lineage)[10] and SOSEKI[7]. Arguably, a prominent manifestation of polar cues in plants is the directional(polar) movement of plant hormone auxin that is mediated by PIN proteins[11]. This polar auxin transport further amplified by auxin (through a positive feedback) is critical for controlling the spatial cues for anisotropic expansion of plant cells[12,13] because auxin causes the weakening of the cell walls, thus promoting cell expansion locally[14,15,16,17]. Consequently, this auxin-mediated cell expansion requires the proper deposition of cytoskeleton elements such as cortical microtubules (CMTs). CMTs contribute to cell polarity maintenance by constraining the directional trafficking of membrane proteins, small signalling molecules and cell wall elements[5,6,18,19], thereby integrating mechanical stresses into the organ morphogenesis[20,21]. Mechanisms of polar auxin transport and CMT deposition are therefore essential for the root development but the integration of these processes is poorly understood.

Computer models are becoming increasingly important tools to provide a mechanistic understanding of processes underlying organ morphogenesis. In the last decade, several computational models of plant development had produced critical insights in the auxin-dependent growth and zonation of mature roots[22–25]. However, most of these models incorporate pre-defined experimental patterns of cell polarities on idealized geometries(e.g. cell grids)[26–30]. While mechanical signals have been shown to be of critical importance to understand the morphogenetic process[31–33], very few mechanics-based models of root meristem growth have been proposed[34–36]. Therefore, the mechanistic understanding of interactions between cell polarities, hormone distribution, cytoskeleton arrangements, and anisotropic cell growth in the root morphogenesis requires the integration of biochemical and mechanical processes at single cell level which remains very challenging[37–39].

To address this challenge we integrated available empirical data on regulation of auxin-dependent cell growth, tissue mechanics, and polar auxin distribution into the cell-based biochemical-mechanical model for the root meristem development. We then used this model to gather mechanistic insights in the *de-novo* establishment of cell polarities and root growth anisotropy from initially non-polar scenario. Our study suggests that a realistic root organization emerges from local interactions between directional transport of auxin, auxin-dependent cell elongation, cell polarization, and biomechanics.

Results

Formulation of design principles underlying root meristem growth

Plant embryogenesis follows the fertilization of the egg, and successive formation of the zygote[40]. The zygote quickly elongates and sets the embryonic axis within a few hours, and after several cell divisions the aerial and root parts are already clearly distinguishable[41]. Most cell types found in the root including the stem cell niche are initiated during the heart developmental stage[42]. Therefore we chose this stage as the initial scenario to simulate the computer model of the *Arabidopsis* root meristem. For that purpose we digitized the microscopy images of an *A. thaliana* embryo by creating 2D embryo meshes with MorphoGraphX[43](Fig. 1A and Supplementary Fig. S1).

We argue that the biochemical-mechanical model based on a minimal set of three biologically plausible principles (**a**-c) could potentially reassemble realistic PIN polarities, auxin distribution and thereby auxin-driven mechanical root growth patterns observed in nature(Fig. 1B):

(**a**), The first design principle relates directly to cell elongation (Fig. 1C). Plant cell walls are under constant internal turgor pressure[14]. Auxin induces cell wall loosening that eventually leads to the cell wall elongation[16]. whereas anisotropic growth requires the proper orientation of CMTs along the cell walls[44,45]. CMTs drive cellulose microfibrils deposition which restrict walls expansion in a specific direction allowing the cell to elongate along a preferred axis[46]. In addition, external mechanical stresses applied on the cell walls organise the orientation of CMTs inside the cell[20,47]. Therefore CMTs self-organize orthogonal to the principal strain direction, restricting cell elongation(Fig. 1C).

(**b**), The second principle defines a default mechanism for cell division(Fig. 1D). Each cell possesses a maximum area attribute, so that when a cell reaches a certain threshold it divides in two daughter cells. The maximum area is specific to each cell type, so that cell size is maintained consistent for each cell lineage(Fig. 1D). The orientation of cell division is always anticlinal and occurs along a division vector passing through the cell centroid and perpendicular with growth anisotropy(Fig. 1D). The only exception applies to the cortex/endodermis initial daughters (CEID) and the epidermis/lateral root cap initials, which divide periclinal and anticlinal/periclinal, respectively, as previously described[4].

(**c**), a third principle describes how auxin transport direction[8] emerges from the dynamic interaction between auxin influx and efflux carriers[11,48], starting from the non-polar scenario(Fig. 1E). While auxin influx carriers of the AUX1/LAX family (Bennett et al., 1998) are typically uniformly distributed around the cell membranes[49], PIN proteins show clear polar subcellular localization(Fig. 1E). Although mechanisms of PIN polarity establishment await further clarification[50], it is generally accepted that auxin plays a critical role in adjusting its own transport by means of a positive feedback mechanism[26]. The theoretical realization of PIN polarization mechanism requires either sensing the net auxin flux through the cell[51–54], auxin concentrations[55–58], auxin gradient inside the cell[59] or a combination of those[60]. Consequently, we considered in our model two complementary strategies for emergent PIN polarization: (1) cells sense the net flux of auxin and adjust accordingly the amount of carriers with-the-flux (also called “auxin-flux method”)[26](Fig. 1E and Supplementary Fig. S2A) (2) auxin passing through a given membrane activates a putative regulator (e.g. general phosphatase) that diffuses across the plasma membrane. This regulator inhibits the polarizing component that activates PINs (e.g. dedicated kinase that phosphorylates PIN) and controls PINs deposition on the membrane (also called “auxin-concentration method”) (Fig. 1E and Supplementary Fig.

S2B). The latter is a molecular realization of auxin flux sensing mechanisms through the action of kinases and phosphatases which recently gathered experimental support[61–63]. We also assumed that CMTs would restrict trafficking of PINs along the axis determined by the principal growth direction(Fig. 1C and 1E).

Taken together, we propose that both mechanical (cell walls strain) and biochemical (polar auxin flow) cues jointly contribute to a feedback mechanism (Supplementary Fig. S3) that could potentially coordinate the morphogenesis of root meristem.

The Root model predicts realistic root tissue geometries, auxin distribution and polar PIN localization patterns

To test whether the proposed set of three principles is indeed sufficient to explain mechanics of anisotropic root growth and associated auxin distribution and PIN polarity, we performed model simulations on the realistic *Arabidopsis* embryo templates(Fig. 1A). Classical approaches to biomechanics such as Finite Element Methods[64,65] pose great challenges in terms of computational efficiency and feasibility when trying to combine complex biochemical reactions with tissue mechanics[66,67]. Alternatively, we developed a biophysical model using an advanced modelling technique called Position-based Dynamics (PBD)[68](Supplementary Fig. S4A). PBD framework is fast, stable and controllable[69] and thus ideal for use in real-time morphogenesis models. The system dynamics are defined by growth constraints that approximate reasonably well physical forces including internal turgor pressure, viscoelastic behaviour of plant cell walls and mechanical deformations (strain) (Supplementary Fig. S4B) (See Supplementary Methods for more information).

Computer model simulations follow the embryo radicle (future root)(Fig. 2B-C and Supplementary Video S1) that is attached to the aerial segment of the plant embryo(Fig. 2A). Auxin is introduced into the vascular tissues and finally evacuated through the epidermis (Fig. 2A), mimicking the auxin flow between the emerging root and the rest of the embryo[70]. In our model, internal turgor pressure competes with cell walls stiffness, maintaining the balance in cell mechanics. Auxin can disrupt this balance by reducing the stiffness of the cell walls, thereby promoting cell wall elongation(Fig. 2B). Simultaneously, PIN localizations spontaneously emerge by sensing auxin flux(Fig. 2 and Supplementary Video S1) or auxin concentrations, respectively(Supplementary Fig. S5 and Supplementary Video S2).

Time-lapse model simulations demonstrate that the proposed set of principles suffice for guiding the transformation of the radicle into a fully grown root meristem, characterized by experimentally observed patterns of anisotropic growth(Fig. 2B and 2D), auxin distribution(Fig. 2C and 2E) and PIN polarization(Fig. 2F-G). Also, model simulations predict the realistic shape of the root tip, resulting from the non-trivial and complex coordination of cell divisions, polarity re-establishment and tissue organization(Fig. 2G). Another interesting finding from model simulations is the presence of a cell growth peak in the apical root meristem(Fig. 2H and 2I), which fits well with recent experimental observations of outgrowing radicle[32]. Predicted asymmetric growth pattern(Fig. 2D and Supplementary Fig. S6) and cell divisions(Fig. 2I) correlate with asymmetric auxin distribution(Fig. 2J), indicating a local modulation of cell growth by auxin(Fig. 2E). Finally, the model predicts details of experimentally observed PIN subcellular localizations(Fig. 2C and Fig. E-G) including apical PIN localization in epidermis and bipolar PIN localization in the cortex(Fig. 2F). Model simulations indicate that this bipolar PIN localization pattern (also observed in nature) would serve an important element of the auxin reflux-loop from the lateral root cap (LRC) towards the internal tissues(Fig. 2F). Finally,

our model captured the precise timing of PIN reestablishment after cell division as observed in experiments(Fig. 2K)[71,72].

Taken together, we show that a minimal set of principles is in principle sufficient to guide the transformation of the radicle into a mature root meristem.

Dynamics of root growth retention requires auxin reflux, local auxin production, and balance in auxin levels

Auxin flow along the root takes two different routes: through the central vascular tissues towards the root tip (acropetal flow) and a reflux back shootward along lateral root cap, cortex and epidermis (basipetal flow)(Fig. 1B and Fig. 2E)[12,73,74]. The auxin maximum is located close to the Quiescent Center(QC)(Fig. 2G) and represents the equilibrium between auxin reaching the root tip from the vascular tissues and auxin leaving the root tip to the outermost tissues. The auxin maximum is necessary for the correct organization of the meristem[75]. Basipetal flow contributes to the regulation of several important processes including elongation zone determination and gravitropism[73,76]. However, it has been suggested that close to the end of the meristem, basipetal auxin flow may reflux back through epidermis and cortex toward the vascular tissues to sustain auxin content of the root meristem even if connection with the shoot was disrupted[12,28,77]. Furthermore, this lateral auxin transport between epidermis and cortex is critical for the growth coordination of adjacent epidermis and cortex tissues[72].

Our model simulations predict the self-organization of reflux phenomenon(Fig. 2G), indicating the presence of lateral auxin traffic from outermost tissues (epidermis and LRC) into the stele(Fig. 2E). Guided by model predictions, we propose that the auxin reflux-loop requires the bipolar deposition of PIN2 proteins in the cortex tissues to redistribute auxin to upper and lower parts of the root(Fig. 2G). To further investigate the importance of the auxin reflux-loop for the sustained growth of the root, we performed model simulations by artificially preventing lateral auxin transport(Fig. 3A-B). We found that a negligible amount of auxin was able to enter the cortex, as no active auxin influx was present, neither bipolar PIN2 localizations in 'no-reflux' simulations(Fig. 3C and Supplementary Video S3) compared to the reference reflux scenario(Fig. 3D and Supplementary Video S3). Strikingly, a lack of auxin recycling in the meristem has no evident outcome on root growth as long as a reliable auxin supply from the shoot is present(Fig. 3E). However, once the root is separated from the rest of the plant (mimicked by removing the auxin influx from the shoot)(Fig. 3A-B, bottom panel), the growth in the no-reflux regime could not be sustained over prolonged time (Fig. 3E) and the auxin content inside the root was eventually lost unless additional auxin was synthesized(Fig. 3F). In contrary, the reflux scenario allows maintenance of auxin levels over prolonged period of time by creating the transient 'memory' of growth which was further prolonged by incorporating an experimentally observed site of auxin biosynthesis in the QC cells(Fig. 3E-F)[78]. These results together indicate that the presence of a PIN-mediated auxin reflux and bipolar PIN localizations in cortex can generate a shoot-independent root growth for extended periods.

Maintaining the correct balance in auxin levels may be important for the sustainable root growth in addition to auxin reflux and auxin production. We next investigated how alterations in auxin levels would modulate the dynamics of root growth patterning. For that purpose, we successively applied external auxin every 6 hours during model simulations (Fig. 4A-B and Supplementary Video S4). Model simulations predict the sequential inhibition and reinstatement of root growth after cyclic auxin removal(Fig. 4C). A similar trend was observed for a shorter period of stimulation(Supplementary Fig. S7A). Notably, these model predictions

223 recapitulate the experimentally-observed temporal inhibition of root growth by external auxin
224 applications[79].
225 Thus, our data indicate that the model can correctly recapitulate experimentally
226 observed oscillatory root growth response to periodically applied auxin. Indeed, the balance
227 in auxin content of the root is critical for the sustained long-lasting growth.
228

229 **Anisotropic growth results from differential expansion at the root-shoot interface**

230 Our model predicts the self-organization of anisotropic meristem growth despite that the auxin
231 effect on cell expansion rate is scalar in individual cells. Notably, model assumes that the root
232 grows faster than hypocotyl: the root-shoot interface (RSI)(Fig. 5A). Recent work suggested
233 that differential cell growth produced by mechanical interactions may regulate organogenesis
234 independently from genetic control, and potentially feedback on it[66,80,81]. To understand the
235 nature of anisotropic growth in our model simulations, we asked whether differential expansion
236 rates at the RSI suffices for the self-organization of CMTs and anisotropic growth.
237 Initially, we simulated the model of root meristem development by integrating a fast
238 growth of both root and RSI, again starting from the embryonic stage(Fig. 5A, Supplementary
239 Video S5). In this scenario, we could only observe the strong isotropic growth of the root
240 without the correct orientation of CMTs(Fig. 5A). However, by assuming a faster growth of the
241 radicle, the model predicts the emergence of a strong anisotropy with clearly visible root
242 polarity axis(Fig. 5B and Supplementary Video S5). We speculate that differential tissue
243 growth could explain the asymmetric expansion of organs through biomechanical
244 arrangements. To test this hypothesis we quantified the growth increase over 6 hour period in
245 radicle and hypocotyl of young seedling using confocal imaging (Fig. 5C)[82]. Indeed, root
246 radicle grew significantly faster that adjacent hypocotyl(Fig. 5D) which is in agreement with
247 our model predictions.
248 We also investigated whether the choice of initial embryo geometry could influence
249 predictions of root anisotropy, auxin distribution and PIN patterns. For that purpose, we tested
250 the model with two other initial templates(Supplementary Fig. S8A-B) derived from published
251 confocal pictures of wild-type embryos of *A. thaliana*[18,83]. Based on the outcome of computer
252 model simulations, we conclude that the particular choice of an initial template has no impact
253 on the self-organization of root growth and auxin distribution, which further confirms our model
254 robustness(Supplementary Fig. S8A-B).
255 In summary, we propose that anisotropic growth can emerge from initially uniform
256 isotropic cell expansion guided by differential growth rates at the RSI. Anisotropic growth
257 further restricts root elongation along a defined axis and maintains PIN polarity.
258

259 **Model simulations recapitulate experimentally observed phenotypes of auxin-mediated**
260 **growth and mechanical stress perturbations**

261 To further test our model robustness we investigated how alterations of auxin transport
262 could impede the patterning dynamics and whether those predictions would match the
263 experimental observations.
264 PIN2 is an important auxin efflux carrier expressed in the most external root tissues:
265 cortex, epidermis and lateral root cap[11]. PIN2 preferentially localizes shootward on the
266 membranes and appears to be involved in auxin reflux from the root tip to the elongation zone[48]

and steers root gravitropic response[84]. PIN2 loss-of-function results in defective gravitropic response largely because of disrupted auxin dynamics[85]. To test whether our model could reproduce the experimental phenotype of *pin2* knockdown mutant, we performed computer simulations by reducing PIN2 expression in epidermis, cortex and lateral root cap(Fig. 6A-B and Supplementary Video S6). The reduced levels of PIN2 produce auxin accumulation in the lateral root cap on both sides of the root(Fig. 6B) unlike the wild-type reference(Fig. 6A). This accumulation of auxin mimics experimental observations of PIN2 knockdown mutant[86]. Similarly, reduced expression of PIN transport in the vascular tissues resulted in severe alteration of auxin distribution and growth defects(Supplementary Fig. S9A and Supplementary Video S7). Finally, we tested how a general knockdown of auxin cellular influx would impact the root growth pattern. As expected, by severely reducing auxin influx root growth was significantly slowed down(Supplementary Fig. S9B and Supplementary Video S8).

Next, we test how local mechanical disruptions of QC, root tip and LRC would alter model outcome and whether this outcome agrees with experimental observations. The QC is a small group of cells (four to seven in the *A. thaliana* root) located in the middle of the root apical meristem[87]. The QC divides infrequently and grows at an extremely low rate[88]. The QC is known to be the source of signals that inhibits differentiation of the surrounding stem cells[89]. QC cells define the correct location of the stem cell niche but also behave as independent cells by self-renewing and replenish initials that have been displaced from their position[90]. QC laser ablation is not lethal for the root as a new QC and stem niche is quickly reconstructed a few cells above the previous one as a consequence of auxin accumulation[91]. We replicated the same experiment *in-silico* by removing the two QC cells from the model after a few hours of simulation(Supplementary Fig. S9C and Supplementary Video S9). Compared to the simulated wild-type (Fig. 6A), the typical auxin accumulation in the root tip is depleted, and auxin reflux in the LRC is significantly reduced, while most of auxin coming from the shoot tends to concentrate in the cells above the lost QC, exactly as observed in experiments[92]. On contrary removal of LRC led to sharp auxin accumulation in the root tip but otherwise fairly normal growth(Fig. 6C and Supplementary Video S10), largely matching empirical reports[93,94].

A. thaliana roots are able to survive not only after QC ablation but even after the complete excision of the root tip, as the plant is able to regenerate a new root tip comprising a complete new root apical meristem[95]. Since the stem cell niche is lost with excision, the regeneration process relies on other pluri-potent dormant cell types available in the remaining stump[96]. We tested if we could replicate this experiment by removing the entirety of the root tip during the simulation(Fig. 6D and Supplementary Video S11). Compared to QC ablation(Supplementary Fig. S9C and Supplementary Video S9), the removal of the root tip displays an even more radical effect on the auxin patterning dynamics(Fig. 6D and Supplementary Video S11). Auxin signal was strongly increased in the vascular tissues and auxin reflux in the lateral tissues was absent; again, model predictions closely match experimentally observed patterns[97,98].

Finally, we explored whether simulated chemical perturbation of cytoskeleton would predict experimentally observed root phenotype. CMTs organization can be modulated by chemical treatments with the chemical agent Oryzalin which cause microtubules depolymerisation and stimulate the radial expansion of roots[98]. We simulated oryzalin treatment by implementing a gradual degradation of CMTs during root growth. For simplicity, we assumed the same sensitivity of cells to oryzalin effect along the meristem(Fig. 6E and Supplementary Video S12). The simulated root growth displays a marked radial swelling, more evident in the centre of the meristem and much less pronounced in the root tip(Fig. 6E). Several cells divide irregularly, as a result of loss of anisotropic growth. As a consequence,

PINs localizations on the membrane became irregular and asymmetric auxin distribution was eventually lost(Fig. 6E). These model predictions are similar to root phenotypes observed after oryzalin treatments[98].

Thus, our framework can be used to predict various root meristem phenotypes including several auxin transport mutants, and mechanical or chemical manipulations of root tissue geometry and thus it is instrumental for focusing new experimental designs in the laboratory.

Discussion

Today, computer models become a central tool for wet-lab scientists to quickly explore possible mechanisms underlying morphogenesis before designing and implementing effective experimental strategies. To date, computer models of root development have been instrumental in understanding root maturation in the context of biochemical flow over non-growing[22,26] or idealized templates[28]. On contrary, little to no attempts were made to couple mechanisms of cell polarity establishment and realistic tissue biomechanics at single cell resolution to mechanistically understand how an organ emerges from small populations of cells.

Here, we implemented an efficient technique called the Position-Based Dynamics[68] to resolve biomechanics of root growth, while simultaneously incorporating detailed biochemical reactions that guide auxin production, distribution and transport at the subcellular level. Our mechanistic cell-based framework successfully predicted the root meristem morphology including tissue patterns, polarity organization, auxin distribution and anisotropic growth from the embryonic onset. Tissue-level properties can emerge from local cell activities and direct cell-to-cell communication through mobile auxin signal with no need for global regulators or polarizers. Anisotropic cell growth and PINs localizations self-organize in complex structures such as root tip and the cortex-epidermis interface. Furthermore our model demonstrates that auxin influx from the LRC and subsequent bipolar PINs localization in the cortex tissues may be important elements of the auxin reflux-loop system. This system can sustains root growth over prolonged time periods, whereas root growth anisotropy would emerge naturally from differential growth rates of adjacent hypocotyl.

Finally, we propose that the network of PIN polarities result from dynamic feedback between auxin passage and biomechanical cues, and suggest a plausible molecular mechanism for cell polarisation based on a putative kinase/phosphatase regulation[61–63,99]. Currently, our model does not address additional mechanisms of root zonation[100], stem cells differentiation[91], and lateral root initiation[101], opening the possibility for modular extensions of the current framework to account for further complexities; for instance the action of other hormones and postembryonic regulatory mechanisms like gravitropism and phototropism.

As the quantitative model predictions are in a fair agreement with experimental observations, our framework will be very useful to predict the phenotypes of various root mutants and test the effects of perturbations such as chemical treatments, gene knockdown or mechanical alterations, thereby fostering the effective design of experiments in the laboratory. This work combines different aspects of morphodynamics and represents a leap forward towards quantitative models of plant organogenesis which could serve as a next-stage platform to develop novel traits of high socio-economic importance.

Materials and Methods

Arabidopsis thaliana embryo cell segmentation

In order to obtained the segmented digital mesh of an embryo template it is necessary to observe the following procedure: 1) Get the microscope picture of an *A. thaliana* embryo without the aerial parts, segmentation is better obtained from pictures with a black background and colour cell borders with high contrast; 2) Load the picture in the MorphoGraphX Stack; 2) Go to the view tab and turn on the cutting surface. Click the grid checkbox and hit reset. It should draw a plan around the image. You can use the sliders to adjust the size; 3) Use the Mesh-Creation-Mesh Cutting Surface process. This will create a mesh in that location. Turn off the cutting surface. 4) Subdivide the mesh a few times; 5) Project signal, using a range like (-1, 1) as the mesh should be in the middle. If the projection is too coarse, subdivide the mesh again; 6) Segment the stack as described in the MorphoGraphX tutorial[43]; 7) Convert the mesh into a cell mesh with Tools-Cell Maker-Mesh 2D-Tools-Polygonize Triangles. Set the "Max Length" parameter to zero; 8) a final pass of smoothing can help to remove the jagged lines from the cells; 9) rescale the mesh to the desired size and save it.

Computational model

The model was created using MorphoDynamX, the next generation of the MorphoGraphX software[43] based on an advance data structure called Cell Complexes[102,103] that overcomes the typical limitations of previous technologies like Vertex-Vertex complexes[104] and are ideal for modelling subdividing geometry in 2 and 3 dimensions. Cells are represented as triangulated polygons obtained through the segmentation process described in the previous section. Cells are composed of vertices connected by edges, and bounding internal faces. Each of these three elements (vertices, edges and faces) has their own biological interpretation and possesses different attributes and properties that allow the model to run and produce a root-like structure. Perimeter edges represent the cell walls while internal edges might be broadly identified as the cell cytoskeleton. The model does not distinguish between cell walls and cell membranes, both are depicted as the same edge but they are computationally distinguished depending on the situation (whether calculating mechanical or chemical effects). Cells at the very top of the model are considered either sources or sinks (in the real heart stage of the embryo auxin flows into the epidermal layer of the upper part and again back into the vascular tissues of the root, creating a auxin loop inside the embryo), so auxin that reaches the top is automatically removed from the system. The mechanical growth of the simulated root is based on Position-Based Dynamics (PBD)[68]. Position-based dynamics is a method used to simulate physical phenomena like cloth, deformation, fluids, fractures, rigidness and much more[69]. PBD allows overcoming the typical limitations of force-based models by omitting the velocity layer and immediately working on the positions following constraints that restrict the systems dynamics in order to obtain a desired effect. Chemical processes are numerically solved using the simple Euler method [105]. Model implementation is described in details in the Supplementary Information section.

Time-lapse confocal imaging of young seedlings

Confocal laser-scanning micrographs of 35S::PIP2-GFP transgenic line were obtained as published elsewhere[82]. Briefly, seeds were stratified for 3 days, seed coat was removed and

peeled embryos were imaged using vertical Zeiss LSM700 microscope with a 488-nm argon laser line for excitation of GFP fluorescence. Emissions were detected between 505 and 580 nm with the pinhole at 1 Airy unit, using a 20x air objective. Images were taken every 20 minutes and Z-stack maximal projections were done using ImageJ software.

Acknowledgments

We are grateful Richard Smith, Anne-Lise Routier, Crisanto Gutierrez and Juergen Kleine-Vehn for providing critical comments on the manuscript. Funding: This work was supported by the Programa de Atraccion de Talento 2017 (Comunidad de Madrid, 2017-T1/BIO-5654 to K.W.), Severo Ochoa (SO) Programme for Centres of Excellence in R&D from the Agencia Estatal de Investigacion of Spain (grant SEV-2016-0672 (2017-2021) to K.W. via the CBGP). In the frame of SEV-2016-0672 funding M.M. is supported with a postdoctoral contract. K.W. was supported by Programa Estatal de Generacion del Conocimiento y Fortalecimiento Cientıfico y Tecnologico del Sistema de I+D+I 2019 (PGC2018-093387-A-I00) from MICIU (to K.W.). MG is recipient of an IST Interdisciplinary Project (IC1022IPC03).

Author Contributions

KW and MM designed the computer model and analysed data. M.M implement model and performed computer model simulations. MM and KW wrote the manuscript with the help from co-authors. MG and EB design and performed time-lapse confocal imaging experiments.

Competing Interest Statement: the authors declare no competing interest

References

1. Friml, J. *et al.* Apical-basal polarity: Why plant cells don't standon their heads. *Trends in Plant Science* vol. 11 12–14 (2006).
2. O'Brien, J. A. A. *et al.* Nitrate Transport, Sensing, and Responses in Plants. *Molecular Plant* vol. 9 837–856 (2016).
3. Chapman, N., Miller, A. J., Lindsey, K. & Whalley, W. R. Roots, water, and nutrient acquisition: Let's get physical. *Trends in Plant Science* vol. 17 701–710 (2012).
4. Choi, J. W. & Lim, J. Control of asymmetric cell divisions during root ground tissue maturation. *Molecules and Cells* vol. 39 524–529 (2016).
5. Yang, Z. Cell polarity signaling in Arabidopsis. *Annual Review of Cell and Developmental Biology* vol. 24 551–575 (2008).
6. Siegrist, S. E. & Doe, C. Q. Microtubule-induced cortical cell polarity. *Genes and Development* vol. 21 483–496 (2007).
7. Yoshida, S. *et al.* A SOSEKI-based coordinate system interprets global polarity cues in Arabidopsis. *Nature Plants* vol. 5 160–166 (2019).
8. Wisniewska, J. *et al.* Polar PIN localization directs auxin flow in plants. *Science (80-.).* **312**, 883 (2006).
9. Duan, Q., Kita, D., Li, C., Cheung, A. Y. & Wu, H. M. FERONIA receptor-like kinase regulates RHO GTPase signaling of root hair development. *Proc. Natl. Acad. Sci. U.*

437 *S. A.* **107**, 17821–17826 (2010).

438 10. Pillitteri, L. J., Peterson, K. M., Horst, R. J. & Torii, K. U. Molecular profiling of
439 stomatal meristemoids reveals new component of asymmetric cell division and
440 commonalities among stem cell populations in Arabidopsis. *Plant Cell* **23**, 3260–3275
441 (2011).

442 11. Adamowski, M. & Friml, J. PIN-dependent auxin transport: Action, regulation, and
443 evolution. *Plant Cell* **27**, 20–32 (2015).

444 12. Paponov, I. A., Teale, W. D., Trebar, M., Blilou, I. & Palme, K. The PIN auxin efflux
445 facilitators: Evolutionary and functional perspectives. *Trends in Plant Science* vol. 10
446 170–177 (2005).

447 13. Overvoorde, P., Fukaki, H. & Beeckman, T. Auxin control of root development. *Cold*
448 *Spring Harbor perspectives in biology* vol. 2 (2010).

449 14. Rayle, D. L. & Cleland, R. E. The acid growth theory of auxin-induced cell elongation
450 is alive and well. *Plant Physiol.* **99**, 1271–1274 (1992).

451 15. Barbez, E., Dünser, K., Gaidora, A., Lendl, T. & Busch, W. Auxin steers root cell
452 expansion via apoplastic pH regulation in Arabidopsis thaliana. *Proc. Natl. Acad. Sci.*
453 *U. S. A.* **114**, E4884–E4893 (2017).

454 16. Majda, M. & Robert, S. The role of auxin in cell wall expansion. *International Journal*
455 *of Molecular Sciences* vol. 19 (2018).

456 17. Peaucelle, A., Wightman, R. & Höfte, H. The Control of Growth Symmetry Breaking in
457 the Arabidopsis Hypocotyl. *Curr. Biol.* **25**, 1746–1752 (2015).

458 18. Nieuwland, J. *et al.* Re-induction of the cell cycle in the Arabidopsis post-embryonic
459 root meristem is ABA-insensitive, GA-dependent and repressed by KRP6. *Sci. Rep.* **6**,
460 (2016).

461 19. Adamowski, M., Li, L. & Friml, J. Reorientation of cortical microtubule arrays in the
462 hypocotyl of arabidopsis Thaliana is induced by the cell growth process and
463 independent of auxin signaling. *Int. J. Mol. Sci.* **20**, (2019).

464 20. Hamant, O., Inoue, D., Bouchez, D., Dumais, J. & Mjolsness, E. Are microtubules
465 tension sensors? *Nat. Commun.* **10**, (2019).

466 21. Hamant, O. & Haswell, E. S. Life behind the wall: Sensing mechanical cues in plants.
467 *BMC Biology* vol. 15 (2017).

468 22. Rutten, J. P. & ten Tusscher, K. In Silico Roots: Room for Growth. *Trends in Plant*
469 *Science* vol. 24 250–262 (2019).

470 23. van Berkel, K., de Boer, R. J., Scheres, B. & ten Tusscher, K. Polar auxin trsansport:
471 Models and mechanisms. *Dev.* **140**, 2253–2268 (2012).

472 24. Morales-Tapia, A. & Ruz-Ramírez, A. Computational modeling of auxin: A foundation
473 for plant engineering. *Front. Plant Sci.* **7**, (2016).

474 25. Wabnik, K., Govaerts, W., Friml, J. & Kleine-Vehn, J. Feedback models for polarized
475 auxin transport: An emerging trend. *Molecular BioSystems* vol. 7 2352–2359 (2011).

476 26. Band, L. R. *et al.* Systems analysis of auxin transport in the Arabidopsis root apex.
477 *Plant Cell* **26**, 862–875 (2014).

478 27. Mähönen, A. P. *et al.* PLETHORA gradient formation mechanism separates auxin
479 responses. *Nature* **515**, 125–129 (2014).

480 28. Grieneisen, V. A., Xu, J., Marée, A. F. M., Hogeweg, P. & Scheres, B. Auxin transport
481 is sufficient to generate a maximum and gradient guiding root growth. *Nature* **449**,
482 1008–1013 (2007).

483 29. Wabnik, K., Robert, H. S., Smith, R. S. & Friml, J. Modeling framework for the
484 establishment of the apical-basal embryonic axis in plants. *Curr. Biol.* **23**, 2513–2518
485 (2013).

486 30. Mironova, V. V. *et al.* A plausible mechanism for auxin patterning along the
487 developing root. *BMC Syst. Biol.* **4**, (2010).

488 31. Routier-Kierzkowska, A. L. *et al.* Cellular force microscopy for in vivo measurements
489 of plant tissue mechanics. *Plant Physiol.* **158**, 1514–1522 (2012).

490 32. Bassel, G. W. *et al.* Mechanical constraints imposed by 3D cellular geometry and
491 arrangement modulate growth patterns in the Arabidopsis embryo. *Proc. Natl. Acad.*
492 *Sci. U. S. A.* **111**, 8685–8690 (2014).

493 33. Hamant, O. *et al.* Developmental patterning by mechanical signals in Arabidopsis.
494 *Science (80-.).* **322**, 1650–1655 (2008).

495 34. Fozard, J. A., Lucas, M., King, J. R. & Jensen, O. E. Vertex-element models for
496 anisotropic growth of elongated plant organs. *Front. Plant Sci.* **4**, (2013).

497 35. Jensen, O. E. & Fozard, J. A. Multiscale models in the biomechanics of plant growth.
498 *Physiology* **30**, 159–166 (2015).

499 36. De Vos, D., Vissenberg, K., Broeckhove, J. & Beemster, G. T. S. Putting Theory to the
500 Test: Which Regulatory Mechanisms Can Drive Realistic Growth of a Root? *PLoS*
501 *Comput. Biol.* **10**, (2014).

502 37. Fletcher, A. G., Osterfield, M., Baker, R. E. & Shvartsman, S. Y. Vertex models of
503 epithelial morphogenesis. *Biophysical Journal* vol. 106 2291–2304 (2014).

504 38. Delile, J., Herrmann, M., Peyriéras, N. & Doursat, R. A cell-based computational
505 model of early embryogenesis coupling mechanical behaviour and gene regulation.
506 *Nat. Commun.* **8**, (2017).

507 39. Brodland, G. W. How computational models can help unlock biological systems.
508 *Seminars in Cell and Developmental Biology* vols 47–48 62–73 (2015).

509 40. Park, S. & Harada, J. J. Arabidopsis embryogenesis. *Methods in molecular biology*
510 *(Clifton, N.J.)* vol. 427 3–16 (2008).

511 41. Kimata, Y. *et al.* Cytoskeleton dynamics control the first asymmetric cell division in
512 Arabidopsis zygote. *Proc. Natl. Acad. Sci. U. S. A.* **113**, 14157–14162 (2016).

513 42. Ten Hove, C. A., Lu, K. J. & Weijers, D. Building a plant: Cell fate specification in the
514 early arabidopsis embryo. *Development (Cambridge)* vol. 142 420–430 (2015).

515 43. de Reuille, P. B. *et al.* MorphoGraphX: A platform for quantifying morphogenesis in
516 4D. *Elife* **4**, 1–20 (2015).

517 44. Baskin, T. I. On the alignment of cellulose microfibrils by cortical microtubules: A
518 review and a model. *Protoplasma* vol. 215 150–171 (2001).

519 45. Baskin, T. I. Anisotropic expansion of the plant cell wall. *Annual Review of Cell and*
520 *Developmental Biology* vol. 21 203–222 (2005).

521 46. Landrein, B. & Hamant, O. How mechanical stress controls microtubule behavior and
522 morphogenesis in plants: History, experiments and revisited theories. *Plant J.* **75**,
523 324–338 (2013).

524 47. Jönsson, H. *et al.* Alignment between PIN1 polarity and microtubule orientation in the
525 shoot apical meristem reveals a tight coupling between morphogenesis and auxin
526 transport. *PLoS Biol.* **8**, (2010).

527 48. Peer, W. A., Blakeslee, J. J., Yang, H. & Murphy, A. S. Seven things we think we
528 know about auxin transport. *Molecular Plant* vol. 4 487–504 (2011).

529 49. Kleine-Vehn, J. & Friml, J. Polar targeting and endocytic recycling in auxin-dependent
530 plant development. *Annu. Rev. Cell Dev. Biol.* **24**, 447–473 (2008).

531 50. Feraru, E. *et al.* PIN polarity maintenance by the cell wall in Arabidopsis. *Curr. Biol.*
532 **21**, 338–343 (2011).

533 51. Mitchison, G. J. A model for vein formation in higher plants. *Proc. R. Soc. London -*
534 *Biol. Sci.* **207**, 79–109 (1980).

535 52. Rolland-Lagan, A. G. & Prusinkiewicz, P. Reviewing models of auxin canalization in
536 the context of leaf vein pattern formation in Arabidopsis. *Plant J.* **44**, 854–865 (2005).

537 53. Feugier, F. G. & Iwasa, Y. How canalization can make loops: A new model of
538 reticulated leaf vascular pattern formation. *J. Theor. Biol.* **243**, 235–244 (2006).

539 54. Stoma, S. *et al.* Flux-based transport enhancement as a plausible unifying mechanism
540 for auxin transport in meristem development. *PLoS Comput. Biol.* **4**, (2008).

541 55. Smith, R. S. *et al.* A plausible model of phyllotaxis. *Proc. Natl. Acad. Sci. U. S. A.* **103**,
542 1301–1306 (2006).

543 56. Jönsson, H., Heisler, M. G., Shapiro, B. E., Meyerowitz, E. M. & Mjolsness, E. An
544 auxin-driven polarized transport model for phyllotaxis. *Proc. Natl. Acad. Sci. U. S. A.*
545 **103**, 1633–1638 (2006).

546 57. Merks, R. M. H., Van de Peer, Y., Inzé, D. & Beemster, G. T. S. Canalization without
547 flux sensors: a traveling-wave hypothesis. *Trends Plant Sci.* **12**, 384–390 (2007).

548 58. Wabnik, K. *et al.* Emergence of tissue polarization from synergy of intracellular and
549 extracellular auxin signaling. *Mol. Syst. Biol.* **6**, (2010).

550 59. Kramer, E. M. Auxin-regulated cell polarity: an inside job? *Trends Plant Sci.* **14**, 242–
551 247 (2009).

552 60. Cieslak, M., Runions, A. & Prusinkiewicz, P. Auxin-driven patterning with
553 unidirectional fluxes. in *Journal of Experimental Botany* vol. 66 5083–5102 (2015).

554 61. Marhava, P. *et al.* A molecular rheostat adjusts auxin flux to promote root protophloem
555 differentiation. *Nature* **558**, 297–300 (2018).

556 62. Hajný, J. *et al.* Receptor kinase module targets PIN-dependent auxin transport during
557 canalization. *Science (80-.).* **370**, 550–557 (2020).

558 63. Michniewicz, M. *et al.* Antagonistic Regulation of PIN Phosphorylation by PP2A and
559 PINOID Directs Auxin Flux. *Cell* **130**, 1044–1056 (2007).

560 64. Fayant, P. *et al.* Finite element model of polar growth in pollen tubes. *Plant Cell* **22**,
561 2579–2593 (2010).

562 65. Bidhendi, A. J. & Geitmann, A. Finite element modeling of shape changes in plant
563 cells. *Plant Physiology* vol. 176 41–56 (2018).

564 66. Kierzkowski, D. *et al.* Elastic domains regulate growth and organogenesis in the plant
565 shoot apical meristem. *Science (80-.).* **335**, 1096–1099 (2012).

566 67. Louveaux, M., Rochette, S., Beauzamy, L., Boudaoud, A. & Hamant, O. The impact of
567 mechanical compression on cortical microtubules in Arabidopsis: a quantitative
568 pipeline. *Plant J.* **88**, 328–342 (2016).

569 68. Müller, M., Heidelberger, B., Hennix, M. & Ratcliff, J. Position based dynamics. *J. Vis.*
570 *Commun. Image Represent.* **18**, 109–118 (2007).

571 69. Toyo'oka, T., Suzuki, A., Fukushima, T. & Kato, M. Hair analysis of histamine after
572 fluorescence labeling by column-switching reversed-phase liquid chromatography with
573 electrospray ionization mass spectrometry and application to human hair. *Anal.*

574 *Biochem.* **333**, 236–245 (2004).

575 70. Möller, B. & Weijers, D. Auxin control of embryo patterning. *Cold Spring Harbor*
576 *perspectives in biology* vol. 1 (2009).

577 71. Glanc, M., Fendrych, M. & Friml, J. Mechanistic framework for cell-intrinsic re-
578 establishment of PIN2 polarity after cell division. *Nature Plants* vol. 4 1082–1088
579 (2018).

580 72. Ötvös, K. *et al.* Modulation of root growth by nutrient-defined regulation of polar auxin
581 transport (in press). *EMBO J.* (2021).

582 73. Rashotte, A. M., Brady, S. R., Reed, R. C., Ante, S. J. & Muday, G. K. Basipetal auxin
583 transport is required for gravitropism in roots of Arabidopsis. *Plant Physiol.* **122**, 481–
584 490 (2000).

585 74. Mravec, J. *et al.* Interaction of PIN and PGP transport mechanisms in auxin
586 distribution-dependent development. *Development* **135**, 3345–3354 (2008).

587 75. Petersson, S. V. *et al.* An auxin gradient and maximum in the arabidopsis root apex
588 shown by high-resolution cell-specific analysis of IAA distribution and synthesis. *Plant*
589 *Cell* **21**, 1659–1668 (2009).

590 76. Petrášek, J. & Friml, J. Auxin transport routes in plant development. *Development*
591 **136**, 2675–2688 (2009).

592 77. Benková, E. *et al.* Local, Efflux-Dependent Auxin Gradients as a Common Module for
593 Plant Organ Formation. *Cell* **115**, 591–602 (2003).

594 78. Stepanova, A. N. *et al.* TAA1-Mediated Auxin Biosynthesis Is Essential for Hormone
595 Crosstalk and Plant Development. *Cell* **133**, 177–191 (2008).

596 79. Fendrych, M. *et al.* Rapid and reversible root growth inhibition by TIR1 auxin
597 signalling. *Nat. Plants* **4**, 453–459 (2018).

598 80. Hong, L. *et al.* Variable Cell Growth Yields Reproducible OrganDevelopment through
599 Spatiotemporal Averaging. *Dev. Cell* **38**, 15–32 (2016).

600 81. Hervieux, N. *et al.* Mechanical Shielding of Rapidly Growing Cells Buffers Growth
601 Heterogeneity and Contributes to Organ Shape Reproducibility. *Curr. Biol.* **27**, 3468-
602 3479.e4 (2017).

603 82. Zhu, Q. *et al.* Root gravity response module guides differential growth determining
604 both root bending and apical hook formation in Arabidopsis. *Dev.* **146**, (2019).

605 83. Scheres, B. *et al.* Embryonic origin of the Arabidopsis primary root and root meristem
606 initials. *Development* **120**, 2475–2487 (1994).

607 84. Rahman, A. *et al.* Gravitropism of Arabidopsis thaliana roots requires the polarization
608 of PIN2 toward the root tip in meristematic cortical cells. *Plant Cell* **22**, 1762–1776
609 (2010).

610 85. Dhonukshe, P. *et al.* Plasma membrane-bound AGC3 kinases phosphorylate PIN
611 auxin carriers at TPRXS(N/S) motifs to direct apical PIN recycling. *Development* **137**,
612 3245–3255 (2010).

613 86. Liu, H. *et al.* AUX1 acts upstream of PIN2 in regulating root gravitropism. *Biochem.*
614 *Biophys. Res. Commun.* **507**, 433–436 (2018).

615 87. Doerner, P. Root development: Quiescent center not so mute after all. *Current Biology*
616 vol. 8 (1998).

617 88. Nawy, T. *et al.* Transcriptional profile of the arabidopsis root quiescent center. *Plant*
618 *Cell* **17**, 1908–1925 (2005).

619 89. Van Den Berg, C., Willemsen, V., Hendriks, G., Weisbeek, P. & Scheres, B. Short-
620 range control of cell differentiation in the Arabidopsis root meristem. *Nature* **390**, 287–
621 289 (1997).

622 90. Kidner, C., Sundaresan, V., Roberts, K. & Dolan, L. Clonal analysis of the Arabidopsis
623 root confirms that position, not lineage, determines cell fate. *Planta* **211**, 191–199
624 (2000).

625 91. Sabatini, S., Heidstra, R., Wildwater, M. & Scheres, B. SCARECROW is involved in
626 positioning the stem cell niche in the Arabidopsis root meristem. *Genes Dev.* **17**, 354–
627 358 (2003).

628 92. Reddy, G. V., Gordon, S. P. & Meyerowitz, E. M. Unravelling developmental
629 dynamics: Transient intervention and live imaging in plants. *Nature Reviews Molecular*
630 *Cell Biology* vol. 8 491–501 (2007).

631 93. Tsugeki, R. & Fedoroff, N. V. Genetic ablation of root cap cells in Arabidopsis. *Proc.*
632 *Natl. Acad. Sci. U. S. A.* **96**, 12941–12946 (1999).

633 94. Blancaflor, E. B., Fasano, J. M. & Gilroy, S. Laser ablation of root cap cells:
634 Implications for models of graviperception. *Adv. Sp. Res.* **24**, 731–738 (1999).

635 95. Efroni, I. *et al.* Root Regeneration Triggers an Embryo-like Sequence Guided by
636 Hormonal Interactions. *Cell* **165**, 1721–1733 (2016).

637 96. Sugimoto, K., Jiao, Y. & Meyerowitz, E. M. Arabidopsis Regeneration from Multiple
638 Tissues Occurs via a Root Development Pathway. *Dev. Cell* **18**, 463–471 (2010).

639 97. Matosevich, R. *et al.* Local auxin biosynthesis is required for root regeneration after
640 wounding. *Nat. Plants* **6**, 1020–1030 (2020).

641 98. Baskin, T. I., Wilson, J. E., Cork, A. & Williamson, R. E. Morphology and microtubule
642 organization in arabidopsis roots exposed to oryzalin or taxol. *Plant Cell Physiol.* **35**,
643 935–942 (1994).

644 99. Weller, B. *et al.* Dynamic PIN-FORMED auxin efflux carrier phosphorylation at the
645 plasma membrane controls auxin efflux-dependent growth. *Proc. Natl. Acad. Sci. U.*
646 *S. A.* **114**, E887–E896 (2017).

647 100. Ivanov, V. B. & Dubrovsky, J. G. Longitudinal zonation pattern in plant roots: Conflicts
648 and solutions. *Trends in Plant Science* vol. 18 237–243 (2013).

649 101. Perianez-Rodriguez, J. *et al.* An auxin-regulable oscillatory circuit drives the root clock
650 in Arabidopsis (in press). *Sci. Adv.* (2021).

651 102. Karwowski, R. & Prusinkiewicz, P. The L−system−based plant−modeling environment
652 L−studio 4.0 The L-system-based plant-modeling environment L-studio 4.0. in
653 *Proceedings of the 4th International Workshop on Functional−Structural Plant Models,*
654 (2004).

655 103. Prusinkiewicz, P. & Lane, B. Modeling morphogenesis in multicellular structures with
656 cell complexes and L-systems. *Springer Proc. Math.* **15**, 137–151 (2013).

657 104. Federl, P. & Prusinkiewicz, P. Virtual laboratory: An interactive software environment
658 for computer graphics. in *Proceedings - Computer Graphics International, CGI 1999*
659 (1999). doi:10.1109/CGI.1999.777921.

660 105. Butcher, J. Runge-Kutta methods. *Scholarpedia* **2**, 3147 (2007).

661

662

663

664 **Figures**

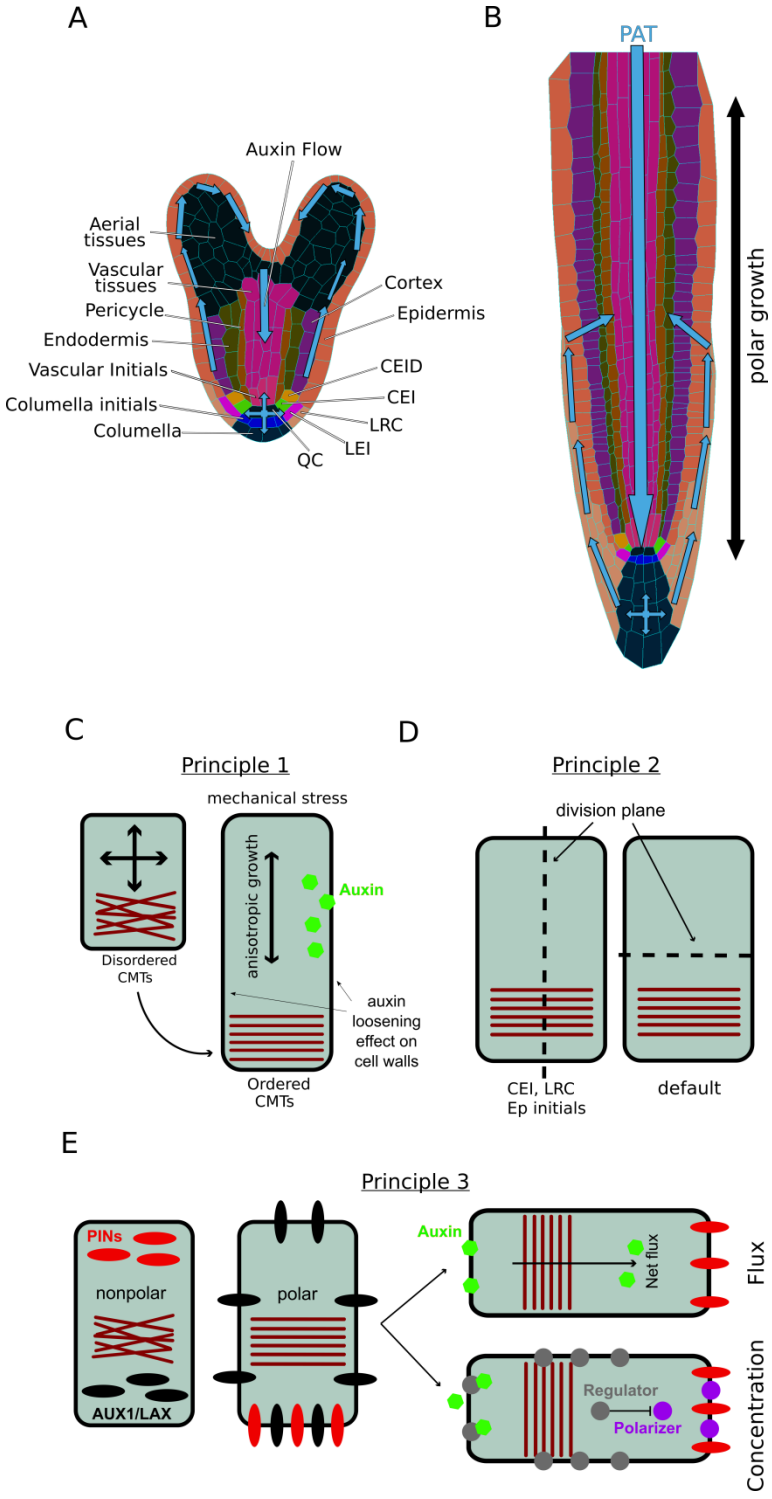

665

666 **Fig. 1 Model purpose and design description.**

667 (**A**) Digitized microscopy image of an *A. thaliana* heart-stage embryo (A) processed through
668 MorphoGraphX[43]. Cell types are shown with different colors, while estimated auxin flow is
669 indicated with arrows. (**B**) Schematics of a mature *A. thaliana* root. The direction of auxin
670 transport is visualized with blue arrows. Growth anisotropy is depicted with a bidirectional
671 black arrow. (**C**) First design principle. Cells are under constant internal turgor pressure. Auxin
672 induces cell walls relaxation and allows cell expansion. External mechanical stress imposed

673 on root cell walls forces the reorganization of the cortical microtubules (CMTs), which in turn
674 generate the anisotropic growth. (**D**) Second design principle - cell division occurs according
675 to the cell polarity defined by CMTs orientation. Cell division plane is orthogonal to cell polarity;
676 exceptions to this rule are cortex/endodermis and LRC/epidermis initials. (**E**) Third design
677 principle. PINs localization is defined by CMTs orientation and auxin flux direction. Auxin
678 feedback on PINs localization is determined by two equivalent mechanisms; the total auxin
679 flux through plasma membrane (the auxin-flux method) or inhibition of PIN polarizer (e.g.
680 kinase) through auxin-driven regulator (e.g. phosphatase) (the auxin-concentration method).

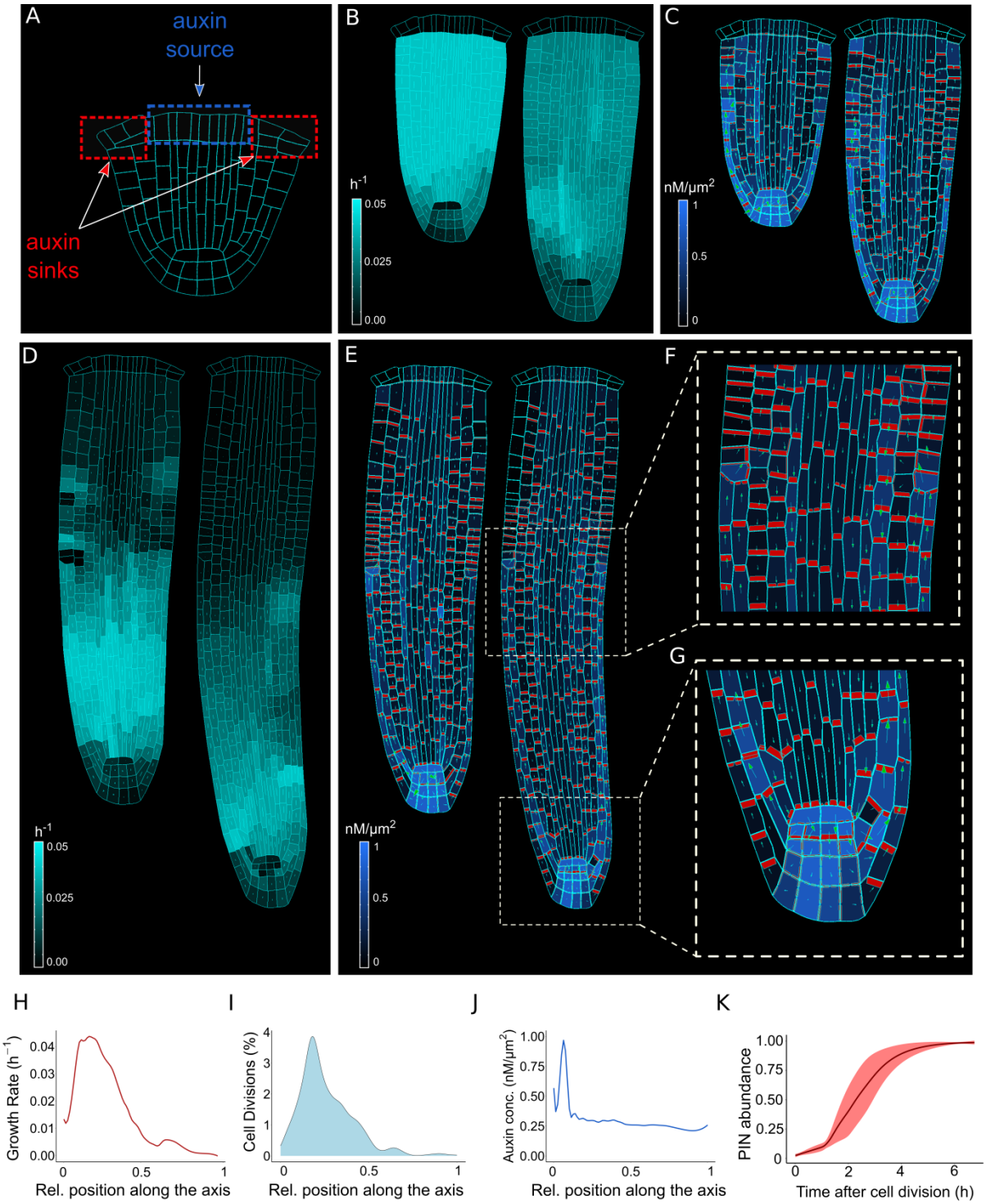

Fig. 2 The model reproduces realistic root meristem geometry, auxin distribution and PINs polar localizations.

(**A**) Initial embryonic setpoint. Locations of auxin influx (auxin source, blue) and evacuation (auxin sinks, red) from the embryo are shown. (**B-E**) Model simulations predict a time evolution of cell growth rates (B and D, bright cyan color) and principal growth directions (white lines). C, E Dynamics of auxin distribution (blue color), auxin flow direction (arrows) and PIN localizations (red). Ongoing cell division events are marked by black regions. (**F, G**) Zoom on basal meristem (F) and root apical meristem (G). The model correctly reproduces very detailed PINs localizations including bipolar PIN2 localization in the cortex (F). (**H**) Growth rate profile

along the root axis. The fastest growing region is located in the apical meristem as observed experimentally[32]. (**I**) Cell division frequencies along the root axis. The majority of cell divisions occur in the apical meristem. (**J**) Auxin gradient along the root axis. Most of auxin is concentrated in the root tip as observed in experiments[13]. (**K**) Time lapse profile of PINs re-localization on the membranes after cell division event. PINs re-localization is completed in approximately 5 hours after cell division[72].

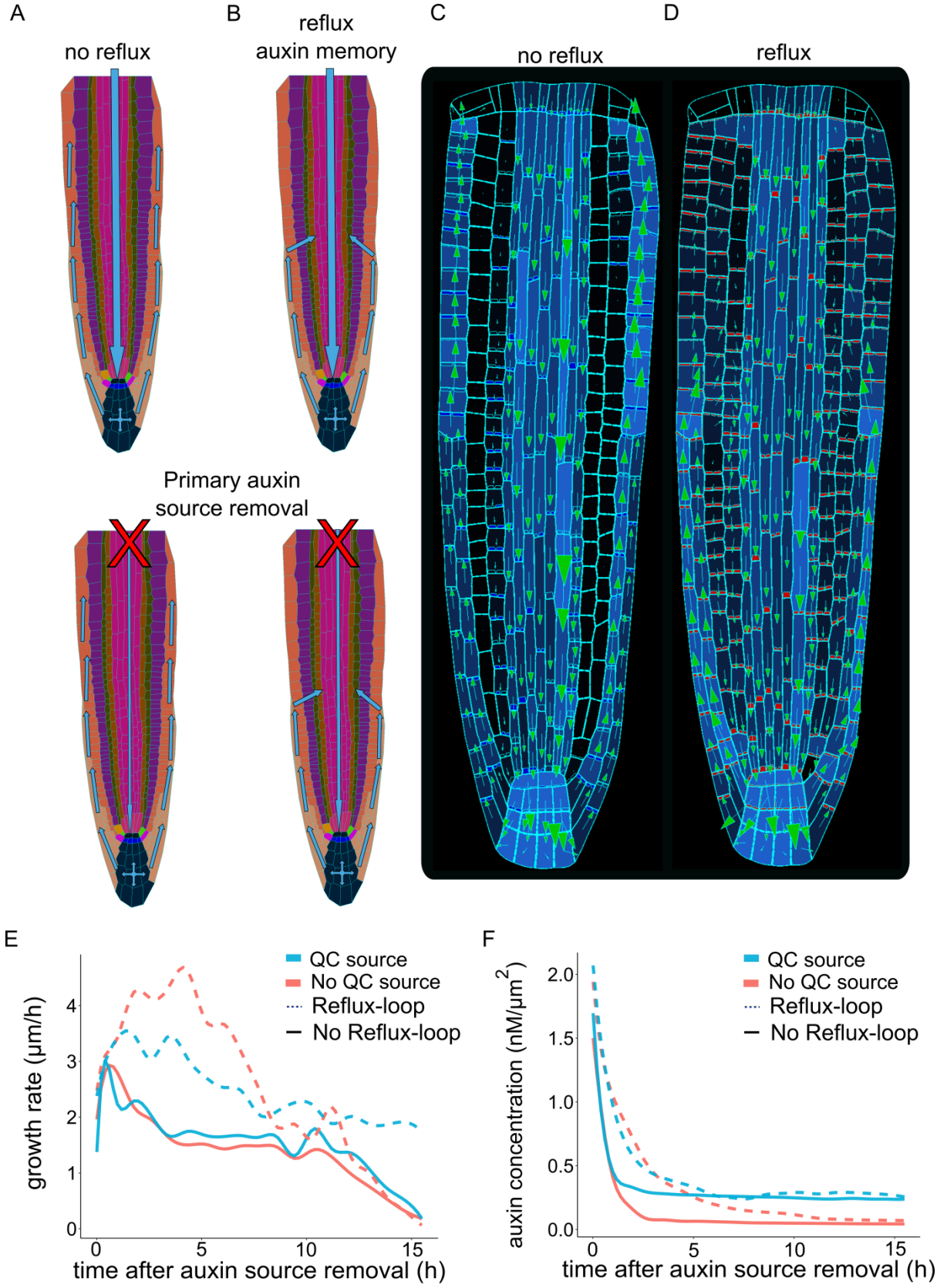

700

701 **Fig. 3 Independent root growth requires auxin reflux and local auxin production**

702 (**A-D**) Schematics (A and B) and model simulations (C and D) with the disabled auxin reflux-
703 loop (A, C) or wild-type-like scenario with self-emerging reflux (B, D). Only in reflux scenario

auxin is permitted to lateralize from the epidermis back into the vascular tissues sustaining the long-term root growth. (**E**) Growth rate profiles of model simulations after primary auxin source removal, in four different scenarios. In the absence of an auxin reflux-loop the root is unable to sustain growth for a long period of time (solid lines) even if a secondary auxin source in the root tip was introduced (solid blue line). On the contrary, the presence of an auxin reflux-loop allows the root to sustain growth for prolonged periods of time (dotted lines), even further augmented by the presence of a secondary auxin source in the root tip (dotted blue line). (**F**) Auxin concentration profiles of model simulations after primary auxin source removal, under different scenarios. In the absence of an auxin reflux-loop the average auxin concentration in the root quickly drops to zero (solid red line). Alternatively, the presence of an auxin reflux-loop allows the root to maintain its auxin reserve for prolonged periods of time (dotted blue line). The presence of a secondary auxin source in the root tip allows the root to further preserve its auxin reservoir for extended period (blue lines).

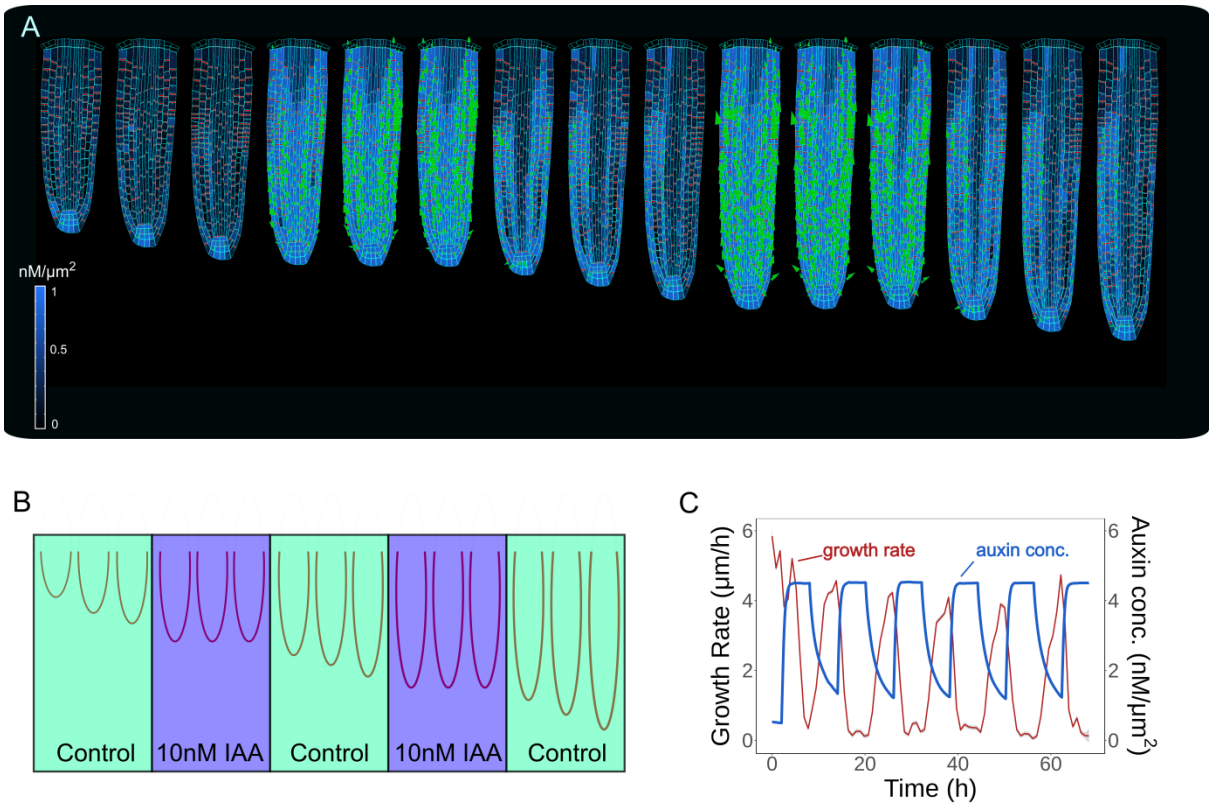

Fig. 4 Model predictions successfully reproduce auxin-dependent reversible inhibition of root growth

(**A**) Successive application of external auxin in model simulations according to a predefined cycle. Root growth is inhibited by the introduction of high amounts of auxin, and subsequently restored after the external application is stopped as seen in experiments[79]. (**B**) Schematic of the *in-silico* experiment. External auxin is uniformly introduced inside the root at predefined time points to inhibit root growth and subsequently removed to allow root growth re-establishment. (**C**) Time lapse profile of root growth rate (red line) and average cell auxin concentration (blue line) monitored during *in-silico* experiment. Introduction of external auxin inhibits root growth rate which is subsequently restored after external auxin is removed.

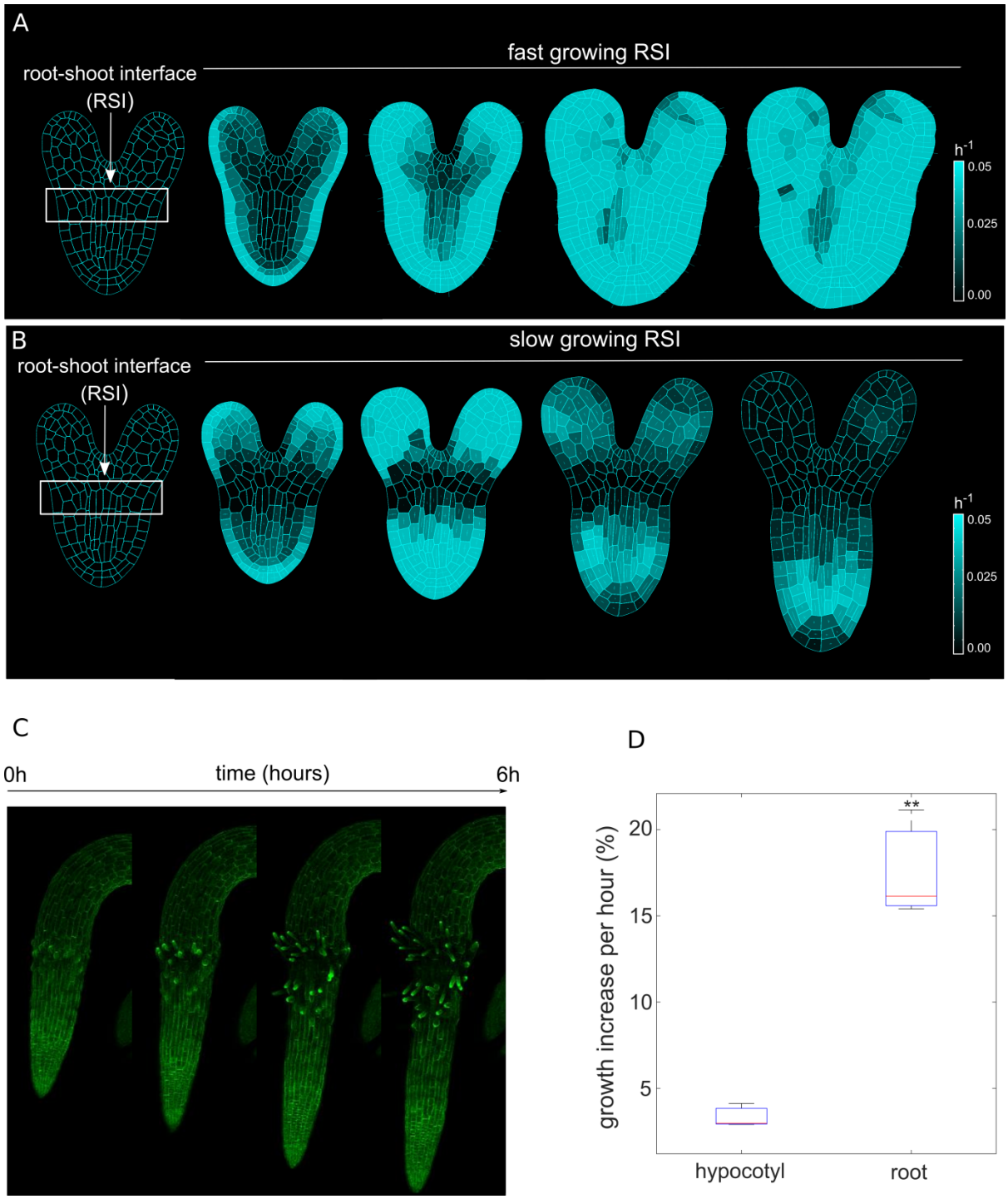

Fig. 5 Differential cell growth at the embryo RSI produces anisotropic expansion of the root

(**A**) Simulated root growth with uniform growth at RSI. The root is unable to achieve independent anisotropic growth since the whole embryo expands isotropically. (**B),** Simulated root outgrowth by assuming differential growth rate at the RSI. Under these conditions the anisotropic growth of the root is self-organizing, later setting the polarity axis. (**C**) Screenshots from time-lapse imaging of growing radicle with PIP-GFP plasma membrane marker[82] for a total time of 6 hours. (**D**) Percentage of growth increase per hour for adjacent organs radicle

741 (root) and hypocotyl quantified from the time-lapse confocal imaging of three independent
742 plants (n=3) . **p-value < 0.015 a one-way ANOVA.
743

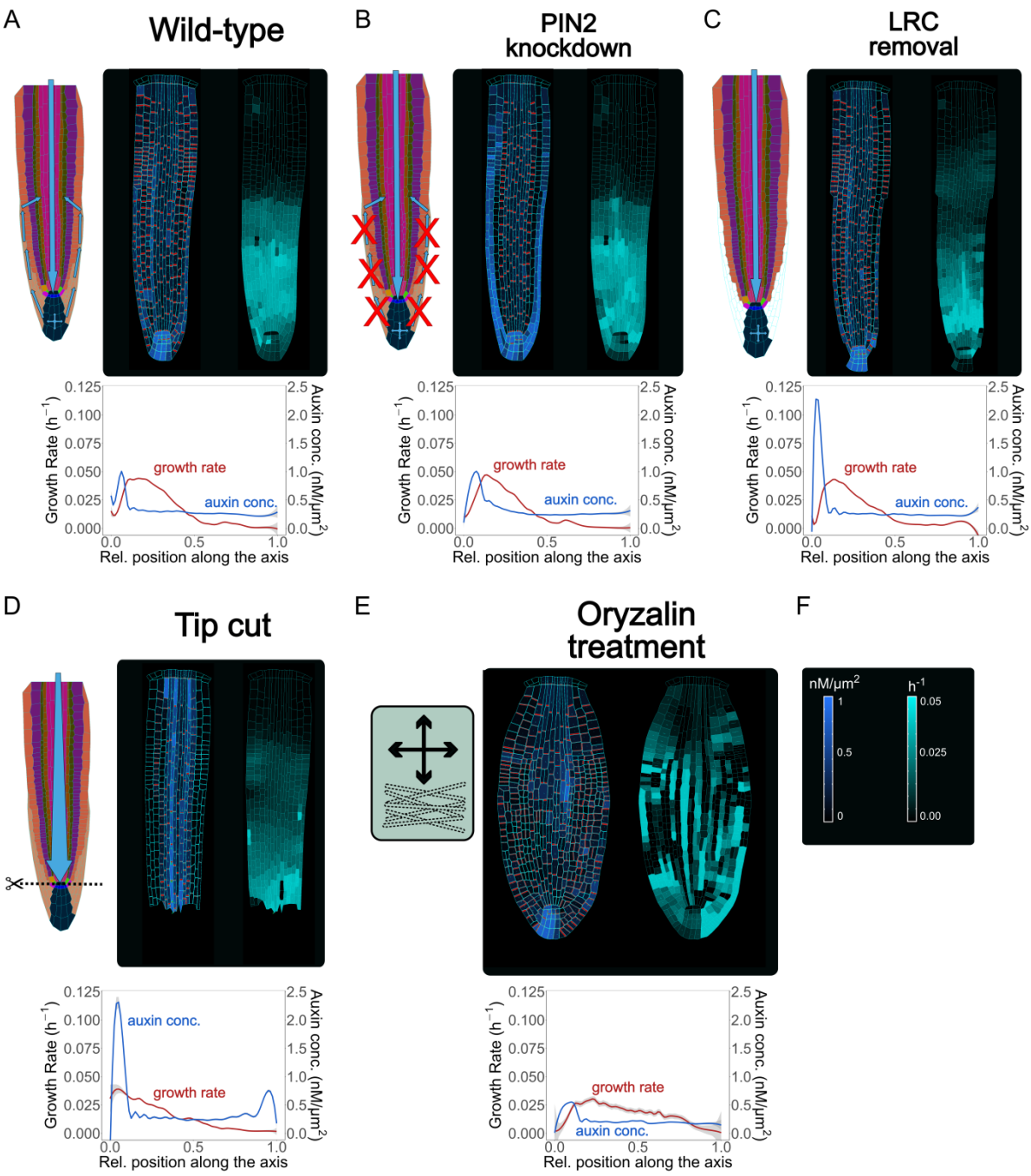

Fig. 6 Model simulations recapitulate experimentally observed phenotypes through genetic, pharmacological and mechanical perturbations

(**A**) Reference model simulation of the wild-type scenario. The figure displays a schematic representation of the auxin flow inside the root (left), auxin distribution and cell growth rate from the model simulations (right), and profiles of auxin concentration (blue line) and growth rate (red line) along the root axis (bottom). (**B**) Model simulation of the *pin2* knockdown mutant. *In-silico pin2* mutant shows strongly reduced PINs expression in the lateral root cap, epidermis and cortex. Note that acropetal auxin flow is severely affected and auxin tends to accumulate in the lateral tissues as observed in experiments[85]. (**C**) Mechanical removal of lateral root cap resulted in the strong accumulation of auxin inside the root tip, largely because auxin cannot flow anymore shootwards through outermost tissues whereas growth rate was not significantly

affected. (**D**) Simulation of root tip cutting. Removing the root tip results in a general increase of auxin level in the central vascular tissues, as a result of the disappearance of acropetal auxin flow. Growth rates profiles demonstrate a significant reduction of root growth by nearly 50%. (**E**) Simulated Oryzalin effect on root growth and polarity. Oryzalin treatment was simulated by inducing a fast degradation of cortical microtubules. Cells lose polarity and growth anisotropy, causing the root to expand and bulge radially as observed in experiments[98]. (**F**) Scale bars of auxin concentration and cell growth rate.

Supplementary Figures

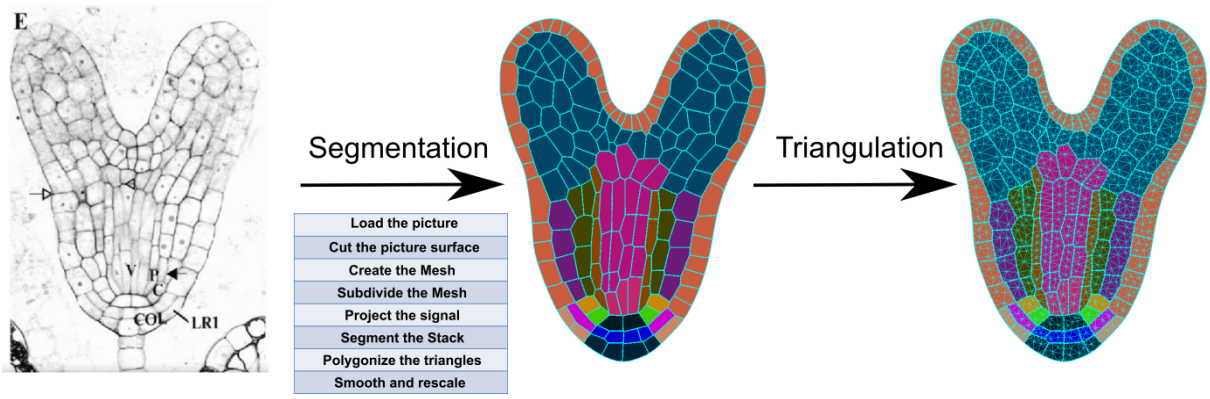

Supplementary Fig. S1 Schematic procedure of the segmentation process that converts the microscopy picture of an A. thaliana embryo into a digitalized mesh.

Microscopy pictures of *A. thaliana* embryo were initially loaded in the MorphoGraphX stack and the signal is projected against a digitalized mesh. Next, the image is segmented to recover the cell boundaries and the resulting mesh is triangulated to obtain an initial embryo template for the model.

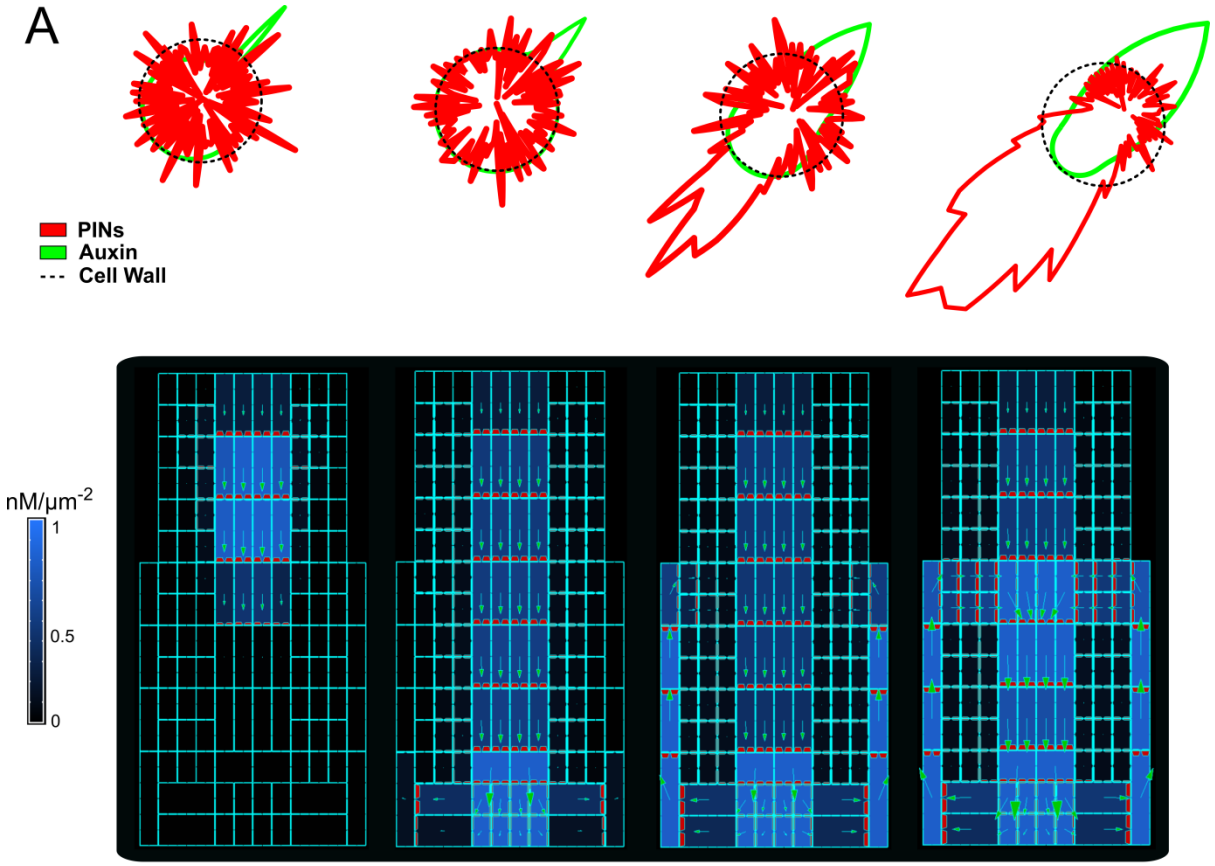
A
PINs
Auxin
Cell Wall
nM/μm-2
1
0.5
0

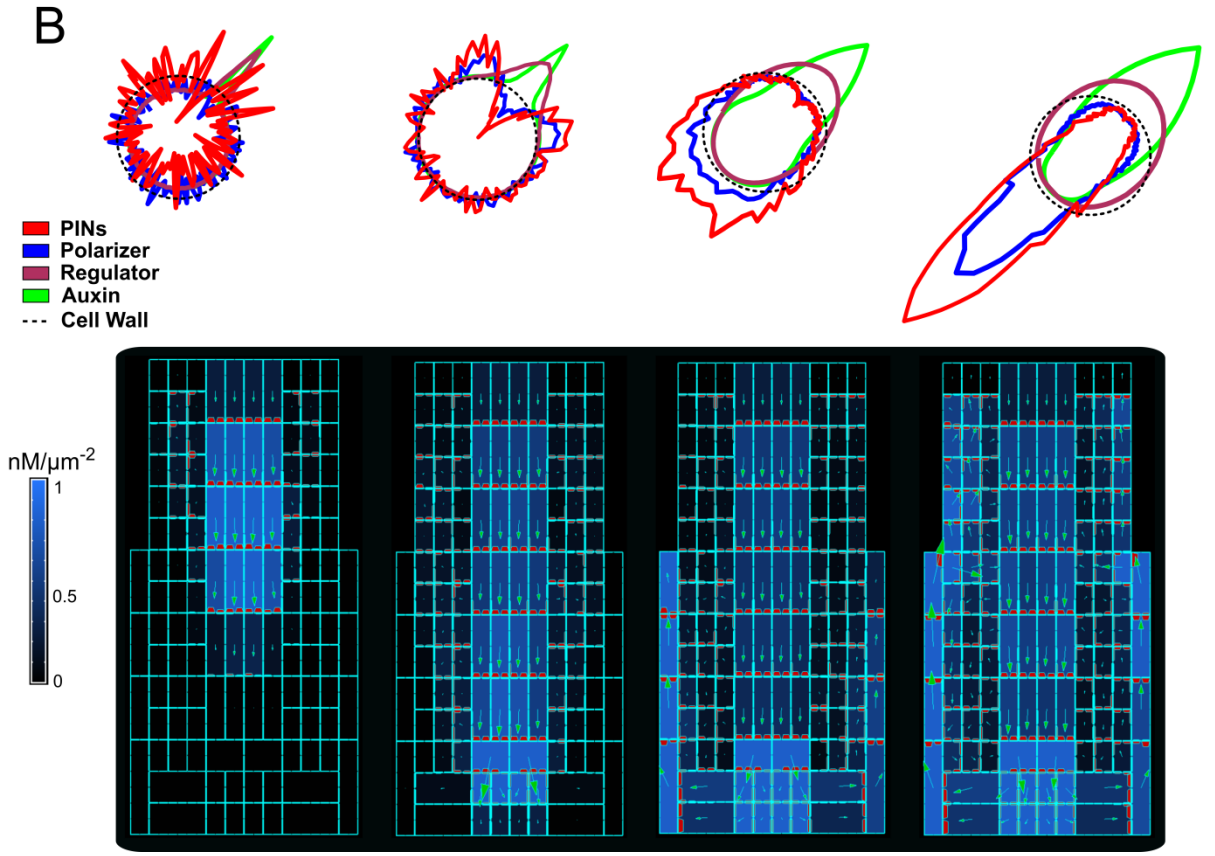
B
PINs
Polarizer
Regulator
Auxin
Cell Wall
nM/μm-2
1
0.5
0

774

775 **Supplementary Fig. S2 Comparison between auxin-flux and auxin-concentration**
776 **methods for PIN polarization.**

777 **(A)** Single-cell model simulation of the auxin-flux method. Auxin application on one side of the
778 cell membrane (green line) induces PINs polarization on the other side of the cell surface. **(B)**
779 Model simulation using the net auxin-flux method (A) on a simplified root-like grid structure.
780 The auxin-flux method is capable of producing a realistic auxin flow inside the grid. Auxin was
781 initially applied to the central cells of the top layer of the grid. (**C)** Molecular realization of flux
782 sensing by the auxin-concentration method. Auxin application on one side of the cell
783 membrane (green line) induces recruitment of regulators proteins which inhibits the PIN
784 polarizer pushing it towards the opposite side of the cell surface. (**D)** Model simulation with the
785 auxin-concentration method (C) on a simplified root-like grid structure. The auxin-
786 concentration method is capable of producing a realistic and stochastic auxin flow inside the
787 root. Auxin was initially applied to the central cells of the top layer of the grid.
788

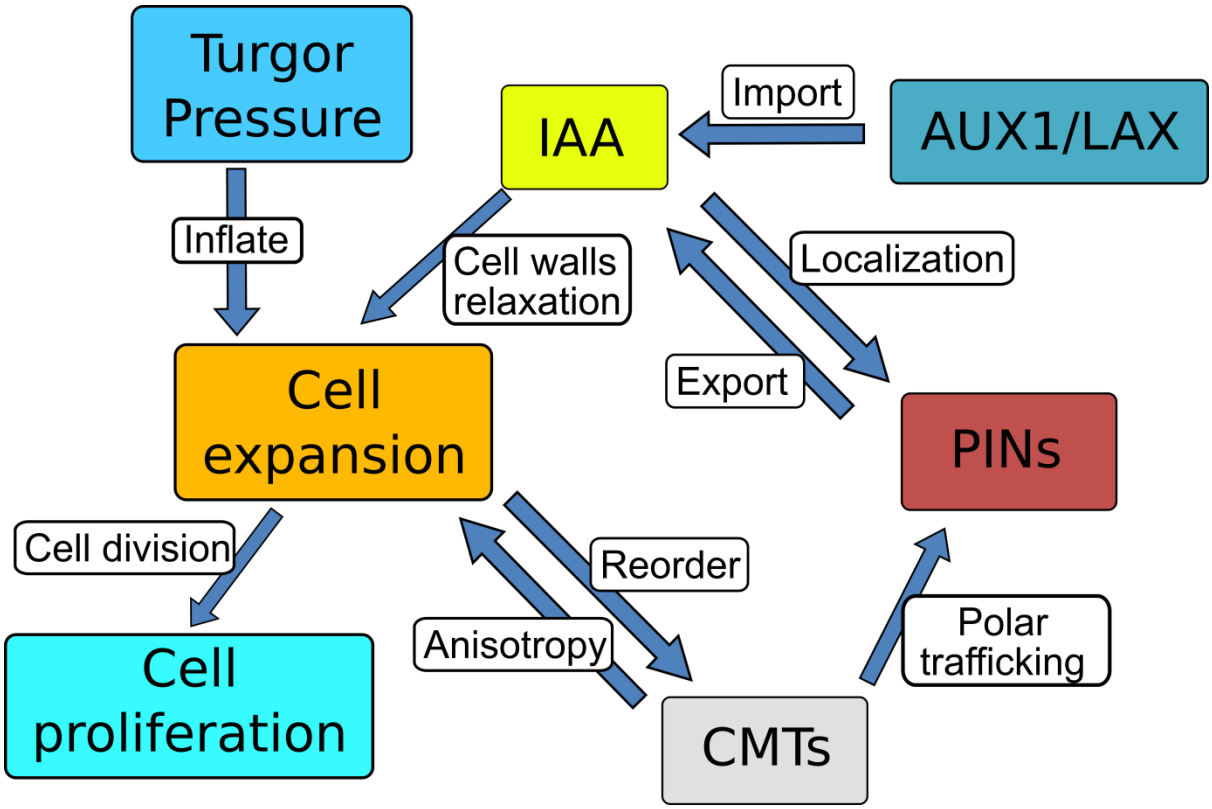

Supplementary Fig. S3 Schematic diagram of the root model.

The diagram shows the main components of the current model and their connections:

- Turgor pressure forces isotropic cell expansion driven by cell wall relaxation induced by auxin.
- Cell expansion causes mechanical stress on the cell walls that triggers cortical microtubules (CMTs) reorganization. Microtubules restrict cell expansion along the axis, causing anisotropic growth.
- Cells divide once the cell area to reach a specific threshold.
- CMTs alignment maintains cell polarity, reinforcing the auxin-dependent PINs polarization.
- Polar PINs efflux carriers and non-polar AUX1/LAX influx carriers mediate the auxin distribution along the root.

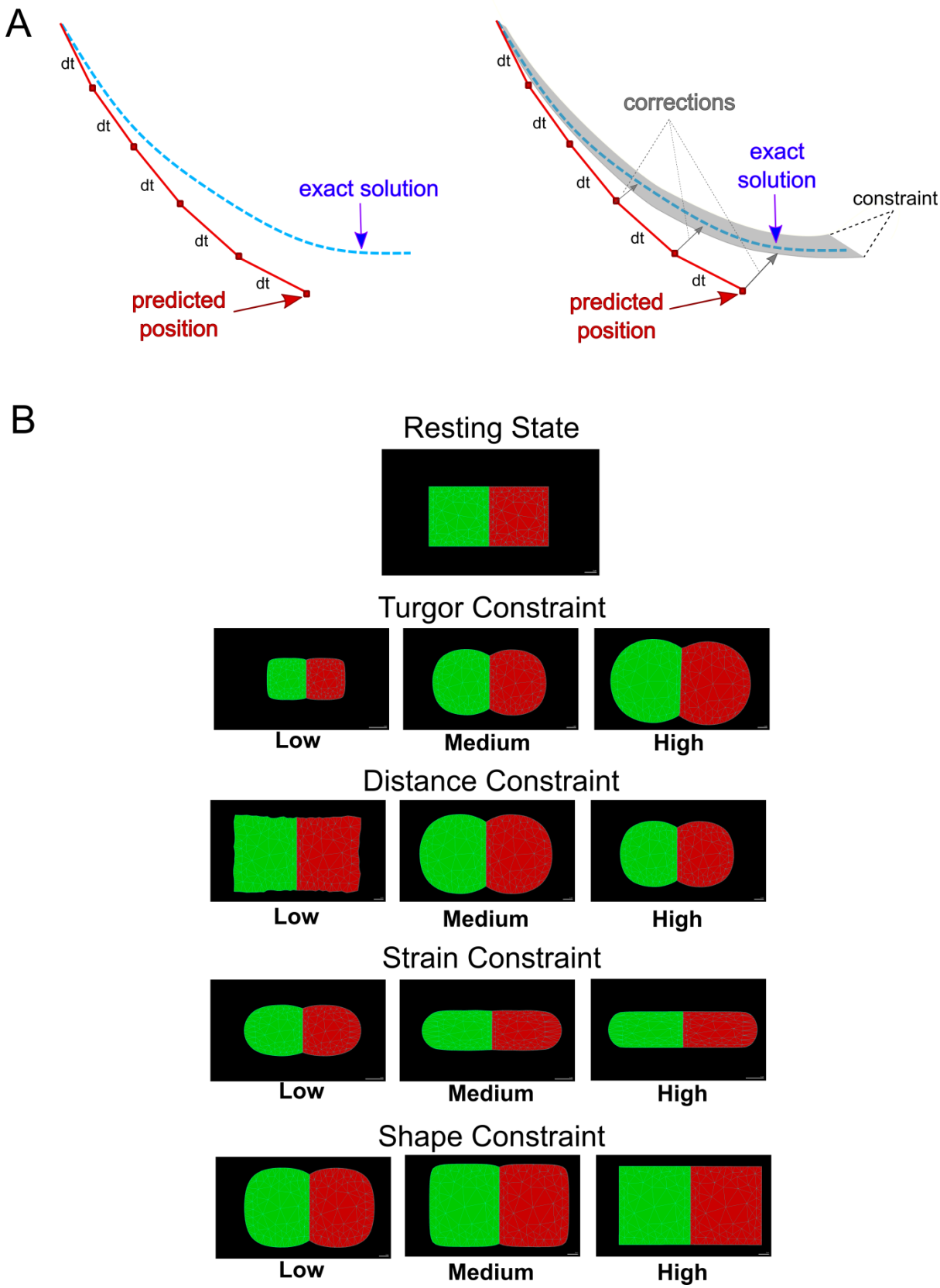

Supplementary Fig. S4 Position-Based Dynamics implementation

(**A**) Comparison between force-based methods (left panel) and position-based dynamics (right panel). In contrast to the typical force-based methods, position-based dynamics skips the

velocity layer and directly works on objects positions in agreement with a determined set of constraints. (**B**) Schematic examples of PBD constraints. Starting from a simple template comprising two squared-shaped triangulated cells, simulations demonstrate the projected effect of each of the constraints implemented in the root model.

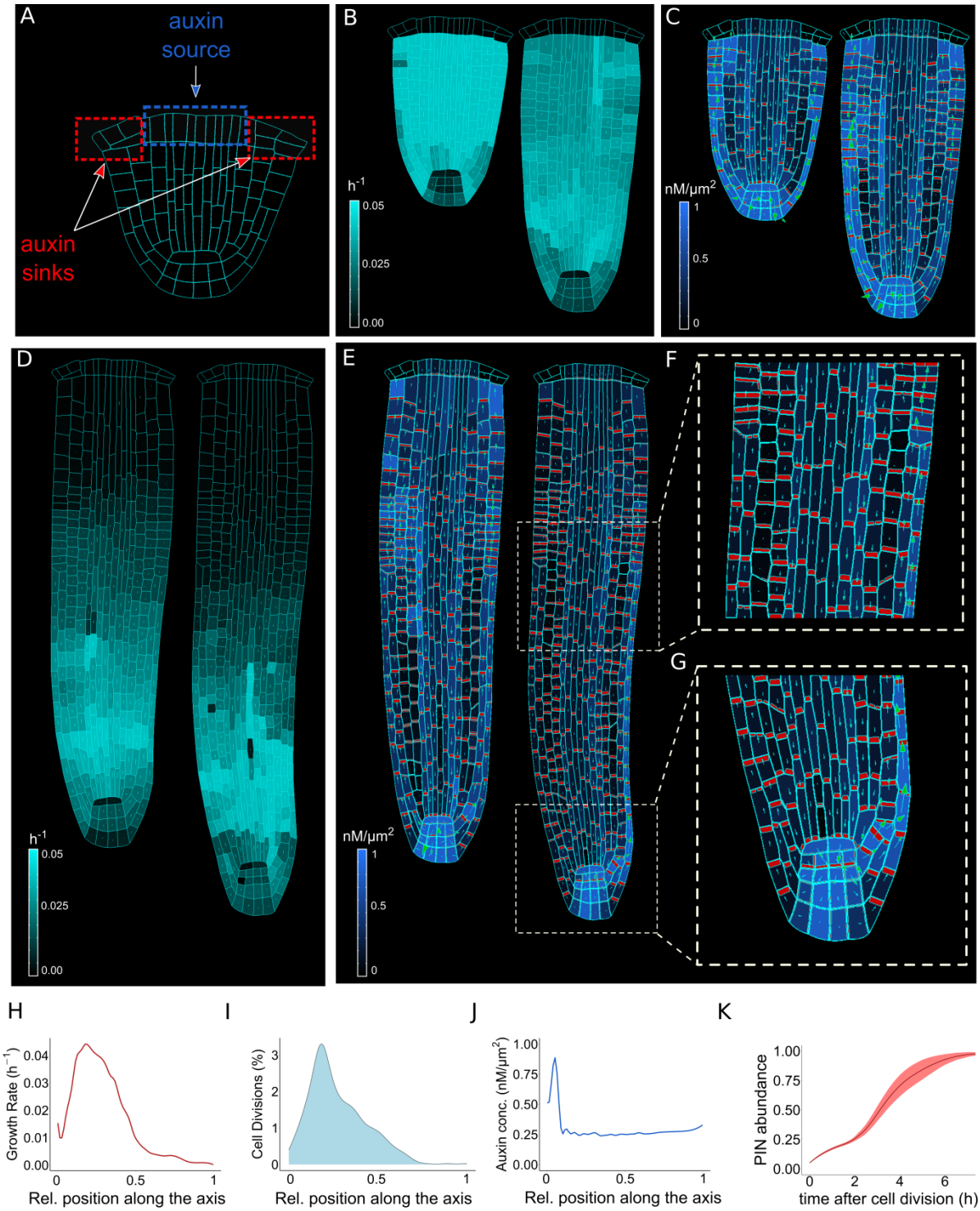

Supplementary Fig. S5 The model is able to reproduce realistic root meristem geometry, auxin distribution and PINs localization. The simulations shown in this figure use the auxin-concentration dependent regulator-polarizer model.

(**A**) Initial model template, indicating the location of auxin influx (auxin source) and evacuation (auxin sinks). (**B, D**) Time lapse of model simulation showing individual cells' growth rate (bright cyan color) and principal growth directions (white lines). (**C, E**) Time lapse of model simulation showing individual cells auxin concentration (blue color) and auxin flow (arrows). (**F, G**) Model simulation close up on basal meristem (F) and root apical meristem (G). The model correctly reproduces experimentally observed PINs localization. Note the bipolar auxin

flow in the cortical tissues (F). (**H**) Growth rate profile along the root axis. The fastest growing region is located in the apical meristem. (**I**) Cell division profile along the root axis. The majority of cell divisions occur in the apical meristem. (**J**) Auxin concentration profile along the root axis. Most of auxin is concentrated in the root tip. (**K**) Time lapse profile of PINs re-localization on the membranes after cell division. PINs re-localization is completed approximately 5 hours after cell division.

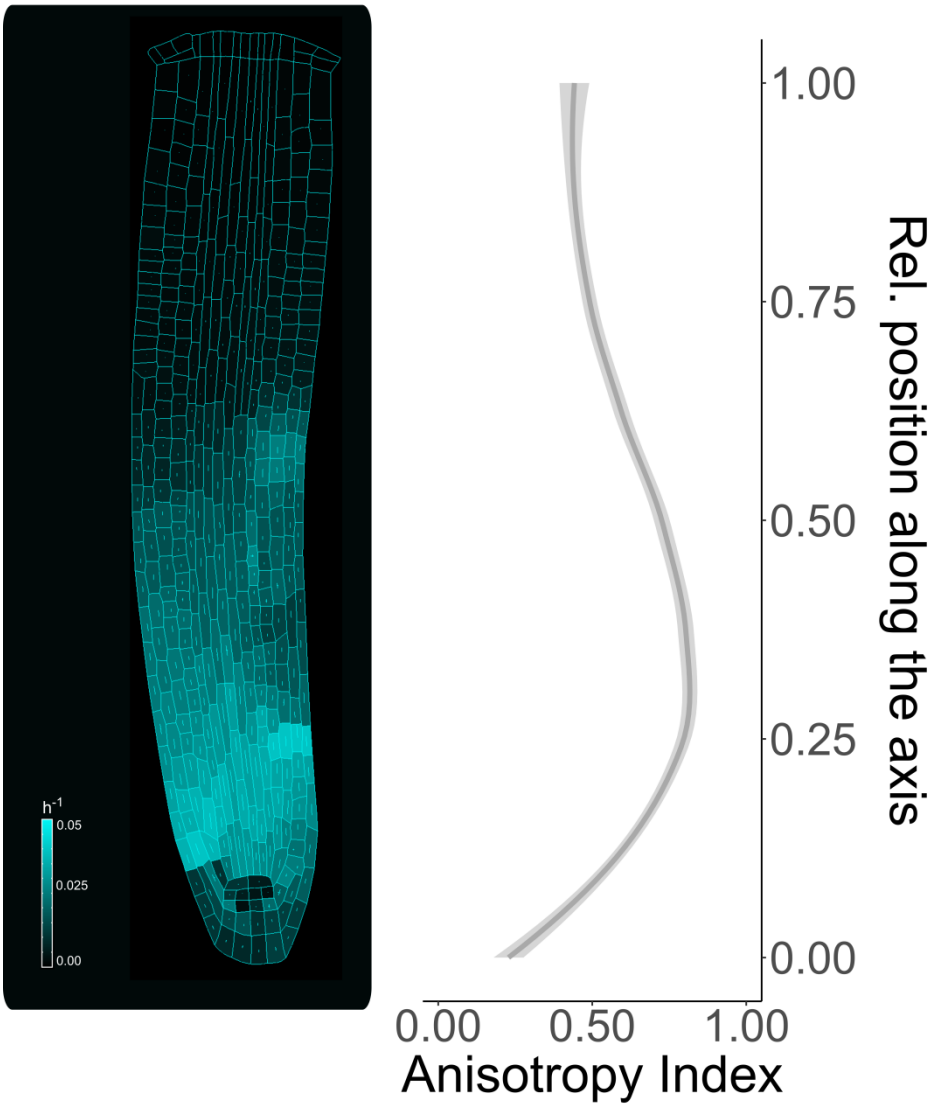

Supplementary Fig. S6 Anisotropy index along the simulated root.

Individual cells growth rate during model simulation (left figure) and anisotropy index along the root axis (right plot). The anisotropy index has been calculated as the difference between two orthogonal vectors representing the amount of cortical microtubules strength inside the cells. A high anisotropy index indicates a greater tendency to anisotropic growth, in contrast to a lower index which denotes a tendency towards the isotropic growth.

A

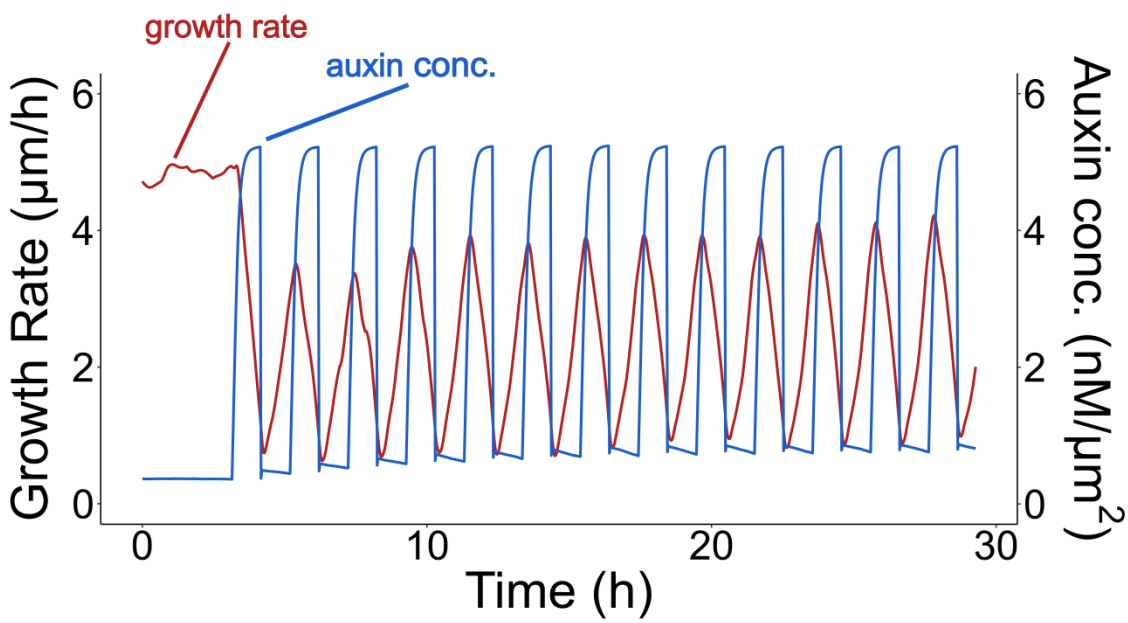

Supplementary Fig. S7 Root growth reversible inhibition by external auxin application.

(**A**) Successive application of 10 nM of external auxin in model simulations according to a predefined cycle of 1 hour. Root growth is inhibited by the introduction of high amounts of auxin, and subsequently restored after the excess of auxin is removed.

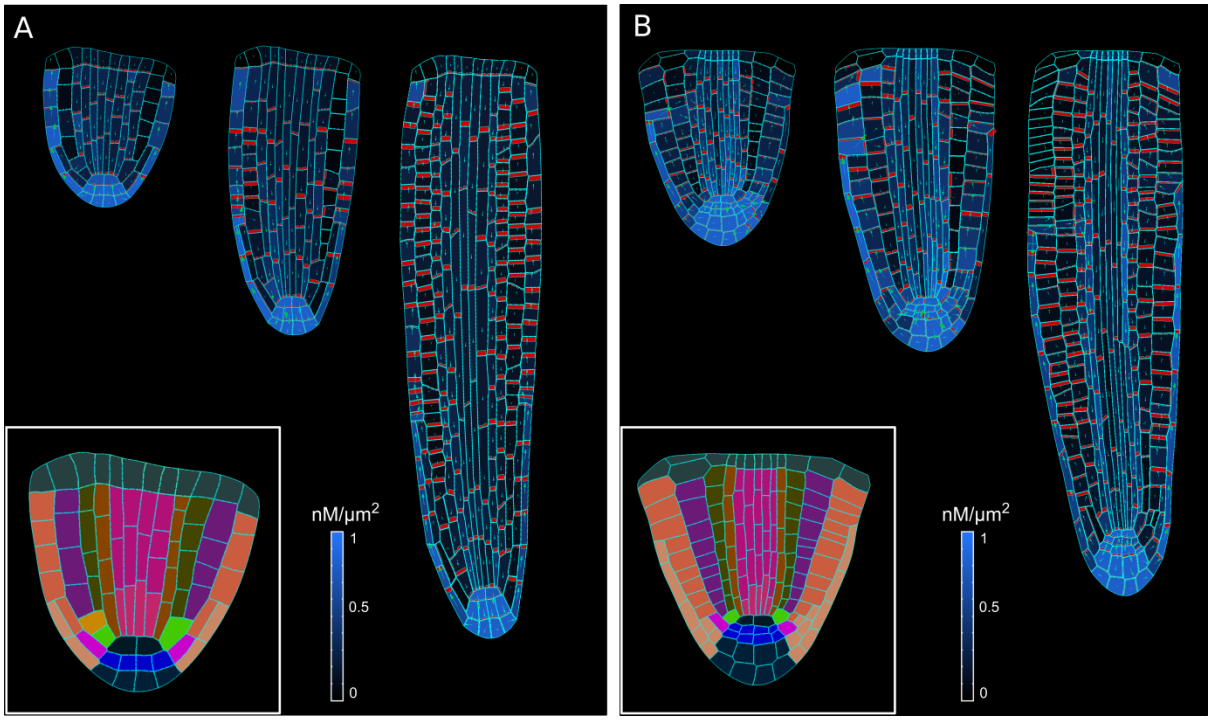

Supplementary Fig. S8 Model simulations using alternative embryo templates.

(**A** ,**B**) Model simulations using alternative embryo templates[18,83]. The particular choice of an initial embryo template has no impact on root self-organization of growth and auxin distribution.

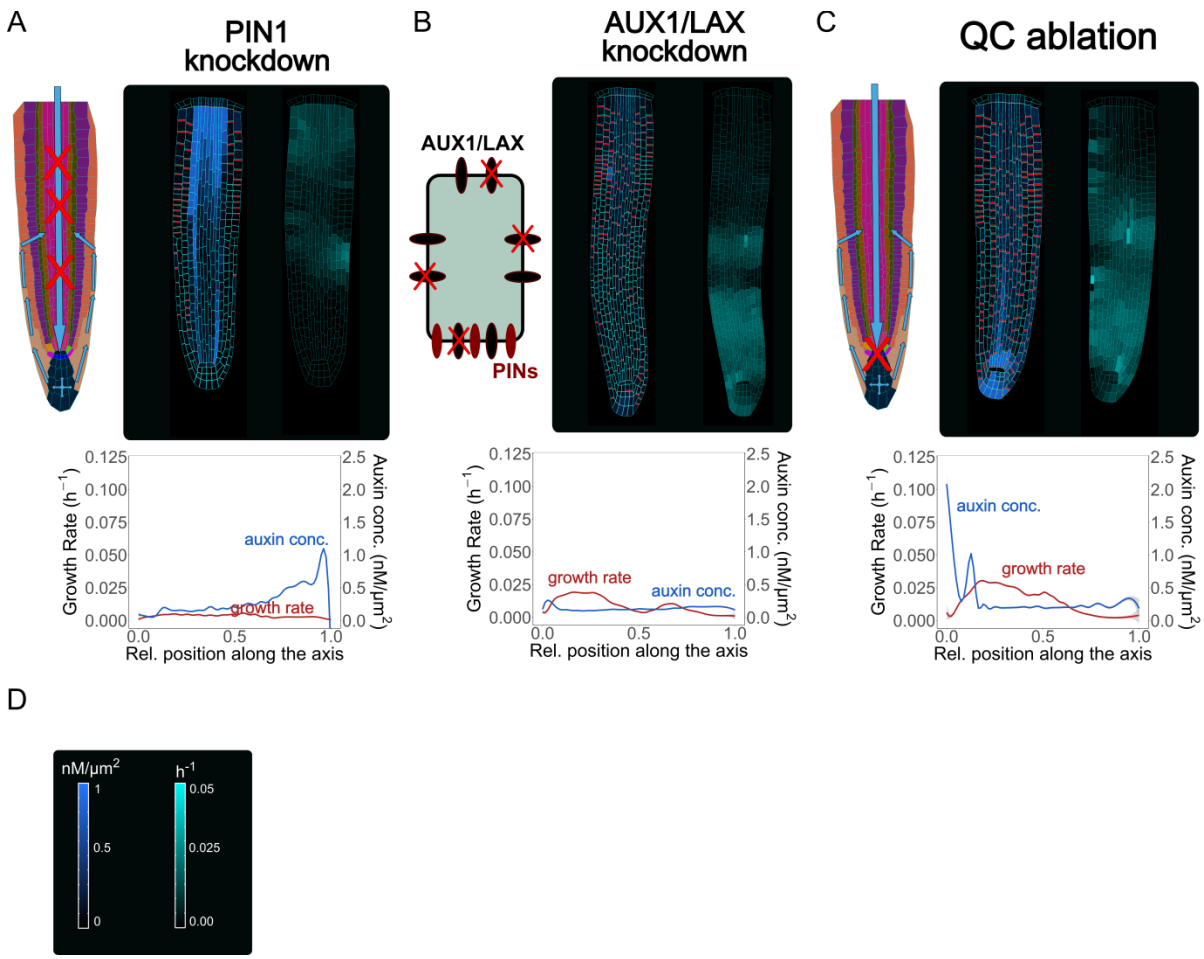

Supplementary Fig. S9 Model simulations recapitulate experimentally observed phenotypes.

(**A**) Model simulation of the *pin1* knockdown mutant. To replicate this type of mutation, PINs expression was reduced by 90% in the vascular tissues, pericycle and endodermis. As it can be observed, auxin levels in the root are strongly depleted as the hormone flow is severely affected by PIN1 down-regulation. (**B**) Simulated *aux1* knockdown mutant. AUX1/LAX expression was reduced by 90% in every cell. This mutant present a striking phenotype as auxin level and root growth are both significantly decreased. (**C**) Model simulation of QC ablation. Removing the QC cells results in an increase of auxin level in the vascular initial cells just above the ablated QC. The model also experiences the disappearance of acropetal auxin flow, as less auxin is able to reach and accumulate in the root tip. (**D**) Scale bars of auxin concentration and cell growth rate.

Supplementary Video Legends

Supplementary Video S1.

Model simulations obtained with the auxin-flux method, related to Fig. 2. The upper simulation displays auxin distribution (blue color), auxin flow direction (arrows) and PIN localizations (red). The lower simulation displays cell growth rate (bright cyan color) and principal growth directions (white lines).

872 **Supplementary Video S2.**

873 Model simulations obtained with the auxin-concentration method, related to Supplementary
874 Fig. S5. The upper simulation displays auxin distribution (blue color), auxin flow direction
875 (arrows) and PIN localizations (red). The lower simulation displays cell growth rate (bright cyan
876 color) and principal growth directions (white lines).

877

878 **Supplementary Video S3.**

879 Model simulations with the enabled/disabled auxin reflux-loop and with/without local auxin
880 production in the QC, related to Fig. 3. Only in reflux scenario auxin is permitted to lateralize
881 from the epidermis back into the vascular tissues, which, together with a secondary auxin
882 source in the QC is able to sustain the long-term root growth even after the removal of the
883 main auxin source from the shoot.

884 **Supplementary Video S4.**

885 Successive application of external auxin in model simulations according to a predefined cycle,
886 related to Fig. 4. Root growth is inhibited by the introduction of high amounts of auxin, and
887 subsequently restored after the external application is stopped. The simulation displays auxin
888 distribution (blue color), auxin flow direction (arrows) and PIN localizations (red).

889 **Supplementary Video S5.**

890 Differential cell growth at the embryo RSI produces anisotropic expansion of the root, related
891 to Fig. 5. The left section simulates root growth with uniform growth at RSI. The root is unable
892 to achieve independent anisotropic growth since the whole embryo expands isotropically. The
893 right section simulates root outgrowth by assuming differential growth rate at the RSI. Under
894 these conditions the anisotropic growth of the root is self-organizing, later setting the polarity
895 axis.

896 **Supplementary Video S6.**

897 Model simulation of the *pin2* knockdown mutant, related to Fig. 6B. In-silico *pin2* mutant shows
898 strongly reduced PINs expression in the lateral root cap, epidermis and cortex. Note that
899 acropetal auxin flow is severely affected and auxin tends to accumulate in the lateral tissues.

900 **Supplementary Video S7.**

901 Model simulation of the *pin1* knockdown mutant, related to Supplementary Fig. S9A. To
902 replicate this type of mutation, PINs expression was reduced by 90% in the vascular tissues,
903 pericycle and endodermis. As it can be observed, auxin levels in the root are strongly depleted
904 as the hormone flow is severely affected by PIN1 down-regulation.

905 **Supplementary Video S8.**

906 Model simulation of the *aux1* knockdown mutant, related to Supplementary Fig. S9B.
907 AUX1/LAX expression was reduced by 90% in every cell. This mutant present a striking
908 phenotype as auxin level and root growth are both significantly decreased.

909 **Supplementary Video S9.**

910 Model simulation of QC ablation, related to Supplementary Fig. S9C. Removing the QC cells
911 results in an increase of auxin level in the vascular initial cells just above the ablated QC. The

model also experiences the disappearance of acropetal auxin flow, as less auxin is able to reach and accumulate in the root tip.

Supplementary Video S10.

Model simulation of lateral root cap ablation, related to Fig. 6C. Mechanical removal of LRC resulted in the strong accumulation of auxin inside the root tip, largely because auxin cannot flow anymore shootward through outermost tissues whereas growth rate was not significantly affected.

Supplementary Video S11.

Model simulation of root tip cutting, related to Fig. 6D. Removing the root tip results in a general increase of auxin level in the central vascular tissues, as a result of the disappearance of acropetal auxin flow.

Supplementary Video S12.

Model simulation of oryzalin effect on root growth and polarity, related to Fig. 6E. Oryzalin treatment was simulated by inducing a fast degradation of cortical microtubules. Cells lose polarity and growth anisotropy, causing the root to expand and bulge radially.

Supplemental Information

Design principles underlying plant root morphogenesis

Contents

1 General Model Assumptions 41
2 Cell Polarization Model 42
2.1 Auxin Transport Model 43
2.1.1 Auxin-flux method 48
2.1.2 Auxin-concentration method 49
3 Root Growth Model 51
4 Physical-based Graphics Implementation 52

1 General Model Assumptions

The root of *A. thaliana* is made of several radially-organized layers of morphologically similar cells that can be easily distinguished by visual inspection of both radial and cross sections[1,2]. The central vascular tissue is composed by a bundle of thin and elongated cells surrounded by the pericycle, a cylindrical sheath protecting the stele. The pericycle is also the origin of emerging lateral organs[3–6]. The central cylinder (stele) is enclosed by three adjacent tissues endodermis, cortex and epidermis. The gravity-sensing columella is located at the very tip of the root and it is composed of four layers of differentiated cells[7,8]. The meristem of the mature root is covered by the lateral root cap which protects the meristem and is periodically shed and replaced by new emerging layers[9,10]. Finally, the root tip stores a group composed of undifferentiated stem cells that divide asymmetrically and replenish the upper sections of individual tissues[11] .Therefore, this precise spatio-temporal arrangement of tissues in the root requires the coordination of cell polarity, anisotropic growth and asymmetric cell divisions. However, mechanisms underlying this coordination are poorly understood.

Auxin-driven root growth of *A. thaliana* has been intensively studied in the last years, and it is known to be one of the major players in root development[12–15]. Auxin distributes along the root through a tightly controlled mechanism and its disruption results in organ growth failure[16–18]. Auxin synthesis and homeostasis is thought to be the other major contributor to cell elongation[19]. The main source of auxin during globular root embryogenesis comes from the shoot, and tends to accumulate in vascular tissue, root tip and epidermis[20,21]. Many aspects of auxin transport by PIN efflux carriers are well understood, however the connections between these mechanisms and the effect on root growth are largely obscure[22–24].

Given the previously described biological properties of *A. thaliana* root, we decided to integrate the following biological observations:

1. The root is composed of cells categorized into different lineages: QC, Columella Initial, Columella, Epidermal/LRC initial, Cortex/Endodermis Initial (CEI), Cortex/Endodermis Initial daughter (CEID), Lateral Root Cap (LRC), Epidermis, Endodermis, Cortex, Pericycle and Vascular. The latter includes all central vascular tissues, for simplicity. Cell types are not uniform and each of them can possess different properties and display specific behaviors[25,26]. For example, each cell type expresses preferentially different PIN protein families[27–29]. These characteristics are discussed in more detail later.

2. Cells are represented as triangulated polygons. Perimeter edges represent the cell walls while internal edges can be broadly identified as the cell cytoskeleton and internal structure. Currently, there is no distinction between cell membranes and cell walls, both are represented by a single edge, which are referred to as “membrane sections” in the text.
3. Cell expansion is described according to the acid-growth hypothesis[30]. Cells are under constant osmotic pressure, and their expansion is prevented by a stiff cell wall with viscoelastic properties. Cells can be considered as incompressible objects. Cell walls possess a strong extensional stiffness at very low or negligible auxin concentration (but also at very high auxin concentration, as discussed later), which prevents the cell from expanding. Auxin (indole-3-acetic acid, IAA), induces acidification of the cell wall activating a range of enzymatic reactions which modifies the extensibility of plant cell walls, allowing the cell to grow[31,32].
4. Mechanical strain induces cortical microtubule (CMTs) orientation and consequently restricts growth, orthogonal to CMTs. It has been shown that mechanical stress can affect microtubules disposition inside the cell[33–35]. Microtubules restrict cell expansion in a determined direction allowing anisotropic growth[36].
5. Cell division occurs according to cell polarity, cell type and condition.
6. Auxin flows into the root from the aerial section of the plant through the vascular tissues [37]. Auxin can also be locally produced in the root apical meristem[38].
7. Auxin is passively diffused inside cells and all over the intercellular space. Auxin is also actively transported by auxin carriers[39]. Auxin exchange between cells is not direct but it occurs through the intercellular space, which is not visually displayed but still considered during modelling computations.
8. Auxin induces PINs and AUX1/LAX protein expression[40]. PINs are subsequently trafficked to the cell membranes according to several criteria as discussed later. Briefly, cell polarity and auxin flux/concentration are the main determiners of PINs localization.

The previous assumptions and their implications are therefore merged into a comprehensive and coherent model structure (Supplementary Fig. S3). Details about each model part are explained in the following sections. Parameters description and value are listed in Supplementary Table S1.

2 Cell Polarization Model

The processes that define cell polarity in plants are not well understood[41,42], and are considered to be different than those in animals. Plant cells display clear polarity patterns when observed to grow anisotropically or by targeting proteins to certain parts of the cell membranes[43]. Root cells present a clear apical-basal (shootward-rootward) polarity, which allows them to elongate towards a determined direction pumping hormones and other molecules creating desired flows[44]. Almost all cell types in *A. thaliana* root display a clear anisotropic pattern[45]. Cell polarity also strongly correlates with PINs localization[46]. Up to the date, several prominent polarity markers have been identified in plants, among those are PIN auxin efflux carriers[47], and putative regulators of cell division orientation BASL[48] and SOSEKI[49]. Regarding PIN proteins, the only known regulators that directly impact on their polarity are the AGCVIII kinases and PP2A phosphatases[50], components of the

phosphorylation on/off switch aimed at the central hydrophilic loop of PINs[51,52]. Auxin transport, mechanical stress, nutrients availability and pathogen response are other processes known to contribute to the cell polarity modulation[24,53–55]. It has been recently shown that external stress can affect internal microtubules organization and therefore guide the cell towards a determined polarity[34]. During root swelling the cells are growing isotropically but also undergo stretching in a direction determined by their geometry and their position inside the organ. According to previous observations, cell microtubules will align perpendicular with the maximal strain, hence enforcing polarity[56]. Once polarity has been clearly determined the cell will acquire anisotropic growth and will enlarge only in a specific direction.

We integrated these findings into a comprehensive polarity system assuming the following:

1. Cortical microtubules orientation restricts the growth anisotropy, orthogonal to the CTMs.
2. External mechanical stresses affect the orientation of microtubules, therefore inducing changes in growth orientation. Microtubules arrange orthogonally to wall strains. In a sense it can be said that the cell "follows" the imposed stress by regulating its own polarity according to the external stresses, using walls strains as reference. Microtubules orientation is represented as a single vector for each cell and, as a consequence, cell polarity can be easily defined as the orthogonal vector to the latter.
3. Cortical microtubules reorientation is triggered only if a certain strain threshold is reached, therefore simulating a plastic behavior.
4. For sake of simplicity, we assume that after cell division newborn cells initially inherit the same CMTs orientation as the mother.
5. Microtubules reorganization is defined by the following formula:

$$\frac{dMF_{cell}}{dt} = MF_{cell} + R_{MF} \cdot \sum_{n}^{mem} \left(n\left(MF_{cell}\right) \cdot \mathrm{abs}\left(n\left(MF_{cell}\right) \cdot v(mem) \cdot \epsilon_{mem} \right) \right) - d_{MF}\, MF_{cell} \qquad (1)$$

MF_{cell} is the vector denoting microtubules orientation inside the cell; R_{MF} is microtubules reorientation rate; $n(MF_{cell})$ is the unit vector parallel to the microtubules vector; $v(mem)$ is the unit vector orthogonal to membrane section *mem*; ϵ_{mem} is the strain rate of membrane section *mem*; d_{MF} is microtubules decay rate.

2.1 Auxin Transport Model

As already discussed in the main text, previously proposed models of auxin polar transport can be approximately divided into two main strategies: flux-based and concentration-based methods[54]. Broadly speaking, flux-based models assume that PIN polarize according to the direction of auxin influx into the cell in order to reinforce the flow in that same direction[57–62]. In concentration-based models it is assumed that the cell is able to detect auxin concentration levels and to trafficking PIN either against or along the gradient[63–66]. A transport feedback model closely related to the flux-based model for venation was proposed a few years ago[67,68]. Despite relying on different formulations, both model types are able to recreate many auxin patterns observed in nature. Phyllotaxis, which creates regularly spaced spots around the

shoot apical meristem, has been modelled both by diffusing inhibitors[69] and reaction–diffusion models[70,71]. However, the models that appear to best represent available data about auxin and its transporters point to a transport-feedback mechanism[63,64,67,72–74]. Phyllotaxis and leaf venation patterns appear very different, and require mechanisms with different properties. Recent years have witnessed the emergence of appealing alternative theoretical hypotheses for polar auxin transport. One of these is the extracellular receptor-based polarization (ERP) model[75]. In this framework, PINs polarity could be regulated by auxin receptors in the apoplast that in turn inhibit local PINs endocytosis after binding auxin. The ERP model easily reproduces several processes like de novo vascularization, venation patterning, and tissue regeneration with only minimal initial assumptions. A mechanistic alternative model was proposed by Jönsson[76]. The author noticed a clear correlation between PINs polarity and the alignment of cortical microtubules, which led him to assume that wall stress induced by auxin accumulation could be involved in determining PINs localization. In the current study we focused on flux-based and concentration-based model alternatives and verified their effect on auxin transport regulation.

In our model both PINs and AUX1/LAX expression is induced by the presence of auxin inside the cell. PIN trafficking to the membranes is also regulated by auxin, while it is kept constant for AUX1. Auxin is exported by PINs from the cell into a virtual intercellular space (not visualized in the simulation), from which it can be imported by AUX1 from neighboring cells. This allows adjacent cells to continuously exchange auxin.

Given the amount of available evidence, we incorporated following assumptions regarding auxin transport in roots:

1. As already discussed, the cell membrane is represented by a two-dimensional polygon. Each edge of the polygon denotes a section of the cell wall/membrane (indicated as *mem* in the following formulas). Each membrane section possesses its own mechanical and chemical attributes, such as PIN and AUX1/LAX amounts, mechanical strain and orientation.
2. Auxin is exported by PINs into the intercellular space and imported by AUX1/LAX:

$$\frac{dI_{mem}}{dt} = K_{AUX1} \cdot AUX1_{mem} \cdot auxin_{mem} \cdot \frac{1}{1\mu m} \quad (2)$$

$$\frac{dE_{mem}}{dt} = K_{PIN} \cdot PIN_{mem} \cdot auxin_{cell} \cdot \frac{L_{mem}}{A_{cell}} \quad (3)$$

$$\frac{dauxin_{mem}}{dt} = \sum_{i}^{n} \left(E_{mem} - I_{mem}\right)_{cell(i)} - \sum_{i}^{m} \frac{D_{auxin}\left(auxin_{mem} - auxin_{mem(i)}\right)}{L_{mem} + L_{mem(i)}} - d_{auxinBase} \quad (4)$$

The intercellular space is always considered to be 1μm thick.

I_{mem} is the amount of auxin imported into the cell through a specific membrane section *mem*; K_{AUX1} is the coefficient of auxin importing rate by AUX1/LAX; $AUX1_{mem}$ is the amount of AUX1/LAX protein localized on membrane section *mem*, $auxin_{mem}$ is the amount of intercellular auxin available by membrane section *mem*; L_{mem} is the length of membrane section *mem*; A_{cell} is the cell area.

E_{mem} is the amount of auxin export from the cell into the intercellular space through a specific membrane section *mem*; K_{PIN} is the coefficient of auxin exporting rate by PIN; PIN_{wall} is the amount of PIN protein localized on membrane section *mem*, $auxin_{cell}$ is the amount of auxin inside the cell; L_{mem} is the length of membrane section *mem*. A_{cell} is the cell area.
$auxin_{mem}$ is the amount of intercellular auxin available by the current membrane section *mem;* $auxin_{mem(i)}$ is the amount of intercellular auxin available by a neighbor of the current membrane section *mem; cell(i)* is one cell sharing the current membrane section *mem*; *mem(i)* is a membrane section neighboring the current membrane section *mem;* D_{auxin} is the auxin diffusion rate in the intercellular space; L_{mem} is length of membrane section *mem;* $L_{mem(i)}$ is length of the neighbor membrane section *mem(i);* $d_{auxinBase}$ is auxin basal degradation rate;

3. Auxin regulates the expression of the auxin carriers[72], by up-regulating PINs and AUX1/LAX expressions:

$$\frac{dAUX1_{cell}}{dt} = AUX1_b + AUX1_{Expr}\left(\frac{\left(\frac{auxin_{cell}}{A_{cell}}\right)^2}{\left(\frac{auxin_{cell}}{A_{cell}}\right)^2 + AUX1_K^2} + \frac{AUX1_{Max}^8}{\left(\frac{AUX1_{cell}}{A_{cell}}\right)^8 + AUX1_{Max}^8}\right) - d_{AUX1}AUX1 \quad (5)$$

$$\frac{dPIN_{cell}}{dt} = PIN_b + PIN_{Expr}\left(\frac{\left(\frac{auxin_{cell}}{A_{cell}}\right)^2}{\left(\frac{auxin_{cell}}{A_{cell}}\right)^2 + PIN_K^2} + \frac{PIN_{Max}^8}{\left(\frac{PIN_{cell}}{A_{cell}}\right)^8 + PIN_{Max}^8}\right) - d_{PIN}PIN \quad (6)$$

$AUX1_b$ is AUX1/LAX basal expression; $AUX1_{expr}$ is the auxin-induced AUX1/LAX maximal expression; $AUX1_K$ is the auxin-induced AUX1/LAX expression coefficient; $auxin_{cell}$ / A_{cell} is the auxin concentration inside the cell; $AUX1_{Max}$ is the maximum concentration of AUX1/LAX permitted inside the cell; $AUX1_{cell}$ / A_{cell} is the current AUX1/LAX concentration inside the cell; d_{AUX1} is AUX1/LAX degradation rate. PIN_b is the PIN basal expression; PIN_{expr} is the auxin-induced PIN maximal expression; PIN_K is the auxin-induced PIN expression coefficient; $auxin_{cell}$ / A_{cell} is the auxin concentration inside the cell; PIN_{Max} is the maximum PIN concentration permitted inside the cell; PIN_{cell} / A_{cell} is the current *PIN* concentration inside the cell; d_{PIN} is PIN degradation rate.

4. Auxin modulates sub-cellular localization of its exporters[77]:

$$\frac{dAUX1_{mem}}{dt} = AUX1_{cell} \cdot AUX1_{tr} \cdot \frac{L_{mem}}{\sum_{n}^{mem} L_{mem}} \cdot \left(\frac{AUX1_{MaxMem}^{10}}{AUX1_{MaxMem}^{10} + \left(\frac{AUX1_{mem}}{L_{mem}}\right)^{10}}\right) - d_{AUX1}AUX1_{mem} \quad (7)$$

$$\frac{dPIN_{mem}}{dt} = PIN_{cell} \cdot PIN_{tr} \cdot PinS_{mem} \cdot \left(\frac{PIN_{MaxMem}^{10}}{PIN_{MaxMem}^{10} + \left(\frac{PIN_{mem}}{L_{mem}}\right)^{10}}\right) - d_{PINmem}PIN_{mem} \quad (8)$$

$AUX1_{mem}$ is the amount of AUX1/LAX proteins trafficked to a specific membrane section *mem*. $AUX1_{cell}$ is the amount of AUX1/LAX available in the cytoplasm; $AUX1_{tr}$

is AUX1/LAX trafficking rate; L_{mem} is the length of membrane section *mem*; $AUX1_{MaxMem}$ is the maximum concentration of AUX1/LAX permitted on one unit of membrane section; $AUX1_{mem}$ is current amount of AUX1/LAX proteins on membrane section *mem*; d_{AUX1} is AUX1/LAX degradation rate.

PIN_{mem} is the amount of PIN proteins trafficked to a specific membrane section *mem*. PIN_{cell} is the amount of PIN available in the cytoplasm; PIN_{tr} is PIN trafficking rate; $PinS_{Mem}$ is the current PINs sensitivity of the membrane section *mem* (see later for a detailed description of this term); PIN_{MaxMem} is the maximum concentration of PIN permitted on one unit of membrane section; PIN_{mem} is current amount of PIN proteins on membrane section *mem*; d_{PINmem} is PIN degradation dynamic formula on the membranes, described as follow:

$$d_{PINmem} = d_{PIN} + \left(d_{PINmax} - d_{PIN}\right) \cdot \left(\frac{1}{1 + \left(\frac{auxin_{cell}}{A_{cell}}\right)^{10}} + \frac{d_s^{10}}{d_s^{10} + PinS_{mem}^{10}} \right) \quad (9)$$

d_{PIN} is the base degradation rate (same as cytoplasmic degradation); d_{PINmax} is the maximum PIN degradation on the membranes; $auxin_{cell}$ / A_{cell} is the current auxin concentration inside the cell; $PinS_{Mem}$ is the current PIN sensitivity for membrane section *mem* (see later for a detailed description of this term); d_s is the level of PIN sensitivity below which maximum PINs degradation is triggered. PINs degradation on the membranes is modelled in this dynamic way in order to allow for a faster turnout of the protein from the membranes when auxin level in the cell is low or the membrane section is no longer sensible to PINs (e.g. the auxin flow has change direction or cell polarity has changed).

5. Auxin can diffuse passively into cells from the intercellular space[37] according to the formula:

$$\frac{dauxin}{dt} = P_{auxin} \cdot \left(auxin_{mem} - auxin_{cell}\right) \cdot \frac{L_{mem}}{A_{cell}} \quad (10)$$

auxin is the amount of auxin that passively enters the cell through membrane section *mem*; P_{auxin} is the membrane permeability; $auxin_{mem}$ is the amount of intercellular auxin available by membrane section *mem*; $auxin_{cell}$ is the amount of auxin inside the cell; L_{mem} is the length of membrane section *mem* and A_{cell} is the cell area.

6. Auxin decays following the combined effect of conjugation and oxidation, at a constant rate[12]. Above a determined concentration threshold of auxin inside the cell, auxin degradation is increased:

$$d_{auxin} = d_{auxinBase} + \left(d_{auxinMax} - d_{auxinBase}\right) \cdot \left(\frac{\left(\frac{auxin_{cell}}{A_{cell}}\right)^{10}}{K_{auxinMax}^{10} + \left(\frac{auxin_{cell}}{A_{cell}}\right)^{10}} \right) \quad (11)$$

$d_{auxinBase}$ is the base auxin degradation rate; $d_{auxinMax}$ is the maximum auxin degradation; $auxin_{cell}/A_{cell}$ is the current auxin concentration inside the cell; $K_{auxinMax}$ is the coefficient for half-max auxin degradation.

7. PINs are trafficked to the membranes according to a specific criterion; Each membrane section *mem*, possesses an instrumental "PIN sensitivity" property, which regulates the propensity of that membrane section to incorporate additional PINs. This property is a proxy for more low-level processes involved in PINs trafficking, like PINs phosphorylation and endocytosis. PIN sensitivity is the linear combination of auxin flow (defined either by auxin flux or auxin concentrations), growth anisotropy (defined by CMTs orientation), and cell geometry. Columella cells are the only exception to this rule; in the columella PINs are always trafficked uniformly among membrane sections, in order to reflect the observed PIN3 distribution[78].
   PIN sensitivity for a given membrane section is defined as:

$$PinS_{mem} = \frac{\exp\left(PinSR_{mem}\right)}{\sum_{n}^{mem_i} \exp\left(PinSR_{mem_i}\right)} \quad (12)$$

$$PinSR_{mem} = kMF \cdot IMF_{mem} + kP \cdot IP_{mem} + kMFP \cdot \left(IMF_{mem} + IP_{mem}\right) + kG \cdot IG_{mem} \quad (13)$$

$$IMF_{mem} = norm\left(MF_{cell}\right) \cdot \left(\frac{U\left(MF_{mem}\right)^4}{U\left(MF_{mem}\right)^4 + Kmf^4} \right); \; U\left(MF_{mem}\right) = n\left(MF_{cell}\right) \cdot n\left(mem\right) \quad (14)$$

$$IG_{mem} = \left(n\left(mem\right) \cdot u\left(axisMax\right)\right) \cdot \frac{\left(1 - \frac{norm(axisMin)}{norm(axisMax)}\right)^4}{\left(1 - \frac{norm(axisMin)}{norm(axisMax)}\right)^4 + Kgeom^4} \quad (15)$$

PIN sensitivity for membrane section *mem* is obtained by applying the soft-max function over all the raw PIN sensitivities calculated for each membrane section of the cell. In equation (13) we define the raw PIN sensitivity for a membrane section *mem*. IMF_{mem} is the contribute of cortical microtubules orientation to PIN sensitivity for membranes section *mem*; kMF_{mem} is the coefficient of contribute of CMTs orientation to PIN sensitivity for membranes segment *mem*; IP_{mem} is the contribute of auxin flow to PIN sensitivity for membranes section *mem* (this parameter depends on the chosen method between auxin-flux and auxin-concentration, see the following section); kP_{mem} is the coefficient of contribute of auxin flow to PIN sensitivity for membranes segment *mem*; $kMFP_{mem}$ is the coefficient of interaction of the two contributes from CMTs

orientation and auxin flow to PIN sensitivity. In equation (14) we define the impact of CMTs orientation (IMF_{mem}) on PIN sensitivity of membranes section *mem*. MF_{cell} is the vector describing CMTs orientation in the cell (described in equation (1)); *Kmf* is the coefficient of half-max contribute of CMTs orientation to PIN sensitivity; $U(MF_{mem})$ is the normalized effect of CMTs orientation on membrane section *mem*, defined as the ratio between the microtubules alignment vector over its norm, multiplied by *n(mem)*, the unit vector orthogonal to membrane section *mem*. In equation (15) we define the impact of cell geometry on PIN sensitivity of membranes section *mem*. *n(mem)* is the unit vector orthogonal to membrane section *mem*; *axisMax* and *axisMin* are the longest and the shortest cell principal axis, respectively; *u(axisMax)* is the unit vector parallel to the longest cell axis; *Kgeom* is the coefficient of half-max contribute of cell geometry to PIN sensitivity.

As discussed before, PIN sensitivity of a specific membrane section is affected either by auxin flux or auxin concentration, depending on the molecular realization. The chosen model will determine the IP_{mem} parameter introduced in the previous section in equation (13).

2.1.1 Auxin-flux method

Flux-based models of auxin transport were first introduced by Sachs[79], which stated that cells sensing the flux of a molecule in a certain direction increases their capacity to transport the molecule in that same direction. This type of strategy is well suited to reproduce situations where auxin displays a strong canalized patterning like in vein formation[80]. Flux-based models assume the existence of cellular flux-sensing mechanisms that have not been discovered so far, and therefore the biological plausibility of these models is a matter of debate. In the auxin-flux model, we calculate the net vector of auxin flow and redirect PINs accordingly. Specifically, the auxin-flux vector is defined as:

$$FLUX_{cell} = \sum_{n}^{mem} u\left(centroid_{cell}, \text{midpoint}_{mem}\right) \cdot \left(I_{mem} - E_{mem}\right) dt \qquad (16)$$

where $centroid_{cell}$ is the centroid of the cell, $midpoint_{mem}$ is the midpoint of membrane section *mem* and $(I_{mem} - E_{mem}) * dt$ indicates the net amount of auxin crossing the membrane section *mem* for a period of time.
Given the auxin-flux vector, the PIN sensitivity contribution by auxin-flow on membrane section *mem* described in equation(13) becomes:

$$IP_{mem} = \left(\frac{FLUX_{mem}{}^{4}}{FLUX_{mem}{}^{4} + Kflux^{4}} \right); \; FLUX_{mem} = norm\left(FLUX_{cell}\right) \cdot \left(u\left(FLUX_{cell}\right) \cdot n\left(mem\right) \cdot L_{mem}\right) \qquad (17)$$

where *Kflux* is the coefficient of half-activation of PIN sensitivity contribution by auxin-flux; $FLUX_{cell}$ is the auxin-flux vector; u($FLUX_{cell}$) is the unit vector parallel to the auxin-flux vector; *n(mem)* is the unit vector orthogonal to the membranes section *mem* and L_{mem} is the length of the membrane section *mem*.

2.1.2 Regulator-Polarizer model

In a concentration-based model the cell is able to sense the difference in auxin concentration between itself and the neighboring cells and allocate PINs on the membrane accordingly[54]. This kind of model assumes the existence of short-distance signaling between cells and is usually designed to work up-the-gradient. Given the fact that such signaling molecules have not been so far discovered, an alternative model was proposed[75] where auxin imported through the cell wall binds to a specific receptor and inhibits endocytosis of PINs from the nearest membrane. This adaptation makes the model more flexible and able to reproduce down-the-gradient auxin flow like in flux-based models, as well as being more biologically sound than auxin-flux models described before.

Starting from this intuition, we developed a concentration-based mechanism for auxin transport capable of reproducing a self-organizing polarization. Cell polarization have been investigated both on theoretical ground[81–85] and designed synthetic circuits[86,87]. In our framework, PIN polarity emerges from the interaction between three molecules: auxin, a polarizer and a regulator. The polarizer is a molecule that promotes sorting of PINs to the membrane section where it is most abundant (e.g. specific kinase that phosphorylates PIN). The regulator is a molecule that is activated by auxin and inhibits polarizer presence on the membranes (e.g. antagonizing phosphatase). Auxin application on a membranes section promotes regulator trafficking on that section, which in turn reduces the presence of the polarizer. Diffusion of the regulator over the surface of the cell results in concentrating the polarizer on the opposite cell side on which auxin was applied. Finally, the polarizer promotes PIN trafficking by tuning the auxin contribution parameter IP_{mem} discussed in equation (13).

The model can be resumed by the following assumptions:

- Regulator and polarizer are expressed and degraded at a constant rate in the cytoplasm. Presence of auxin inside the cell promotes trafficking of the two molecules to the membranes.
- Auxin active import across the membranes is sensed by the cell in order to determine the auxin gradient needed to promote regulator binding to the membrane. Auxin gradient for a specific membrane section *mem* is calculated as:

$$Grad_{mem} = \left(\frac{\left(I_{mem} - E_{mem}\right)dt}{1\mu m} + \sum_{n}^{mem_i} \frac{\left(I_{mem_i} - E_{mem_i}\right)dt}{d_{mem_i}} \right) \cdot \frac{1000}{area_{cell}} \qquad (18)$$

  Where $(I_{mem} - E_{mem}) * dt$ indicates the net amount of auxin crossing the membrane section *mem* for a period of time; d_{mem_i} is the distance of membrane section mem_i from our reference membrane section *mem*, calculated as the Euclidean distance between the two sections midpoints. The metrics is further normalized dividing by the cell area and multiplied by 1000.
- Regulator and polarizer diffuses along the cell membrane according to the following equations:

$$D\left(REG_{mem}\right) = D_{REG} \cdot \sum_{mem \pm 1}^{mem_i} \left(REG_{mem_i} - REG_{mem}\right) \tag{19}$$

$$D\left(POL_{mem}\right) = D_{POL} \cdot \sum_{mem \pm 1}^{mem_i} \left(POL_{mem_i} - POL_{mem}\right) \tag{20}$$

D(POL$_{mem}$) and *D(REG$_{mem}$)* are the amount of regulator and polarizer diffused over the membrane, respectively; D_{reg} and D_{pol} are regulator and polarizer diffusion rate, respectively; *POL$_{mem}$* and R*EG$_{mem}$* are the amount of regulator and polarizer on membrane section *mem*, respectively; The polarizer is displaced by the presence of regulator molecules towards the zone where the concentration of the regular is the lowest. To achieve this, we apply a simple stochastic algorithm: for a given membrane section *mem*, a fixed batch amount of polarizer is reserved for possible displacement; then one of the two adjacent membrane segments is selected randomly; if the selected segment contains less amount of regulator than the current segment, the batch of polarizer is moved to that segment, otherwise, nothing is performed. Polarizer displacement can be resumed by the following formula:

$$G\left(POL_{mem}\right) = Kdisp_{POL} \cdot if\left(REG_{mem+i} > REG_{mem} \;\; then \;\; POL_{mem+i} \;\; else \; 0\right)$$
$$i = \text{random}\left(-1, +1\right) \tag{21}$$

where *G(POL$_{mem}$)* is the amount of polarizer displaced by the regulator and *Kdisp$_{POL}$* is the polarizer displacement rate.

- Finally, the amount of molecules present on a specific membrane section *mem* is defined by the following equations:

$$\frac{dPOL_{mem}}{dt} = \tag{22}$$

$$POL_{cell} \cdot Kpol_{tr} \cdot \frac{L_{mem}}{\sum_{n}^{mem_i} L_{mem_i}} \cdot \left(\frac{\left(\frac{auxin_{cell}}{A_{cell}}\right)^2}{\left(\frac{auxin_{cell}}{A_{cell}}\right)^2 + Kpol_{IAA}^2} \cdot \frac{POL_{MaxMem}^{10}}{POL_{MaxMem}^{10} + \left(\frac{POL_{mem}}{L_{mem}}\right)10} \right) +$$

$$+ D\left(POL_{mem}\right) + G\left(POL_{mem}\right) - dPOL \cdot POL_{mem}$$

$$\frac{dREG_{mem}}{dt} = \tag{23}$$

$$REG_{cell} \cdot \left(Kreg_{tr} + Kreg_{GradT} \cdot \left(\frac{Grad_{mem}^4}{Grad_{mem}^4 + Kreg_{GradK}^4}\right)\right) \cdot \frac{L_{mem}}{\sum_{n}^{mem_i} L_{mem_i}} \cdot \left(\frac{\left(\frac{auxin_{cell}}{A_{cell}}\right)^2}{\left(\frac{auxin_{cell}}{A_{cell}}\right)^2 + Kreg_{IAA}^2} \frac{REG_{MaxMem}^{10}}{REG_{MaxMem}^{10} + \left(\frac{REG_{mem}}{L_{mem}}\right)10} \right) +$$

$$+ D\left(REG_{mem}\right) - dREG \cdot REG_{mem}$$

$Kreg_{tr}$ and $Kpol_{tr}$ are regulator and polarizer trafficking rates, respectively; REG_{cell} and POL_{cell} are regulator and polarizer cytoplasmic amounts, respectively; $Kreg_{IAA}$ and $Kpol_{IAA}$ are regulator and polarizer half-max trafficking activation by auxin, respectively; L_{mem} is the length of the membrane section *mem*; IAA_{cell} is the amount of auxin inside the cell; $area_{cell}$ is the cell area; $D(POL_{mem})$ and $D(REG_{mem})$ are the net amount of regulator and polarizer diffused by membrane section *mem*, respectively; $G(POL_{mem})$ is the net amount of polarizer displaced by the regulator on membrane section *mem*; *dPOL* and *dREG* are regulator and polarizer decay rate, respectively; $Kreg_{GradT}$ and $Kreg_{GradK}$ are regulator maximum trafficking rate on membrane and half-max coefficient activation by auxin, respectively.

- Given the calculated amount of polarizer on a given membrane, the auxin flow contribution parameter IP_{mem} on PIN sensitivity described in equation (13):

$$IP_{mem} = \left(\frac{POL_{mem}^4}{POL_{mem}^4 + Kpol_{IP}^4} \right) \tag{24}$$

where $Kpol_{IP}$ is the half-max activation of auxin flow contribution on PIN sensitivity by polarizer amount POL_{mem}.

3 Root Growth Model

The classical morphogen gradient model dictates that the cell fate is regulated by the positional information encoded in different morphogen levels at different positions across a static tissue[88]. However, in a growing system, cells are displaced quickly along the tissue hence varying their exposure to morphogens concentration depending on their current distance for the morphogens source(s). Moreover, cell growth dilutes morphogens concentration and influences their effect on cell regulation. The current model tries to address these issues by monitoring the combined effect of cell growth and morphogens concentration on root development. The proposed model for root growth includes the following assumptions:

1. Cells expand according to the chemiosmotic theory of auxin transport[30]. Cells are under constant turgor pressure which is resisted by the elastic effect of cell walls. In the current model osmotic pressure is realized by a specific position-based dynamics constraint described in the following section.
2. Increasing auxin concentration induces the relaxation of the cell walls allowing cell expansion under the effect of turgor pressure. On the contrary, high auxin levels disable cell walls relaxation[89]. The relationship between cell walls stiffness and auxin is expressed by the following formula:

$$kE_{wall} = kE_{Max} \cdot \left(\frac{K_{1auxin}^4}{K_{1auxin}^4 + \left(\frac{auxin_{cell}}{A_{cell}}\right)^4} + \frac{\left(\frac{auxin_{cell}}{A_{cell}}\right)^8}{K_{2auxin}^8 + \left(\frac{auxin_{cell}}{A_{cell}}\right)^8} \right) \quad (25)$$

kE_{wall} is the extensional stiffness of the cell wall; kE_{Max} is the maximum stiffness a cell wall can achieve; K_{1auxin} is the auxin-induced cell wall relaxation coefficient; K_{2auxin} is the auxin-induced cell wall stiffening coefficient; *auxin/area* is the auxin concentration inside the cell.

3. Cell growth is directionally constrained by the action of cortical microtubules, which, depending on their orientation, make anisotropic growth possible[45]. During model simulation the action of cortical microtubules is made possible by the action of a specific strain-based dynamics constraint (see following section). For a given cell, the strain stiffness of a single wall segment depends on its alignment with cortical microtubules: the closest the alignment the harder the stiffness. This rule prevents the expansion of cell walls that are constrained by microfibrils.
4. Cell division occurs when a certain area threshold is reached. The cell division plane passes through the centroid of the cell polygon and it is orthogonal to the cortical microtubules. As already discussed before, microtubules orientation defines growth anisotropy, and therefore the division line is defined accordingly. Cells divide symmetrically into two cell of the same type of the mother. There are however exceptions to the previous rule, which are justified by experimental observation and tailored to certain conditions:
    a. Cortical/Endodermis Initials Daughters (CEID) cells always divide parallel to cell polarity, to generate one cell of the same type and one CEID cell[90,91].
    b. Cortical/Endodermis Initials Daughters (CEID) divide asymmetrically to generate one endodermal cell and one cortical cell[90,91].
    c. Epidermis/Lateral Root Cap initials alternatively divide either parallel and orthogonal to cell polarity in order to produce lateral root cap cells or epidermal cells, respectively[7].
    d. Quiescent cells divide rarely[25,92,93], and therefore for sake of simplicity we assume that they never grow or divide.
    e. Columella initials divide asymmetrically to generate one cell of the same type and one columella cell[94].
    f. Vascular initials divide asymmetrically to generate one cell of the same type and one vascular cell[95].

4 Physical-based Graphics Implementation

The typical approach to simulate dynamic growing systems in biology is based on force calculations[96].Tissues are usually represented as triangulated meshes made of connected vertices and forces are accumulated on these vertices following specific biological criteria such as internal turgor pressure, anisotropic expansion or gravity. Vertex acceleration is later derived from these forces and vertex masses according to Newton's second law. A time integration scheme is then used to first compute the velocities from the accelerations and then the final positions from the velocities. Classical integration methods are usually unstable or

very computationally expensive, resulting in either unmanageable or extremely inefficient simulations. Therefore, instead of a forced-based system we decided to implement the mechanical growth of *Arabidopsis thaliana* root using Position-Based Dynamics (PBD)[97]. PBD is a recent method used to simulate physical phenomena like cloth, deformation, fluids, fractures, rigidness and much more[98]. PBD omits the velocity layer and immediately works on the positions following constraints that restrict the systems dynamics in order to obtain a desired effect. PBD main loop inside the model code can be summarized by the following diagram:

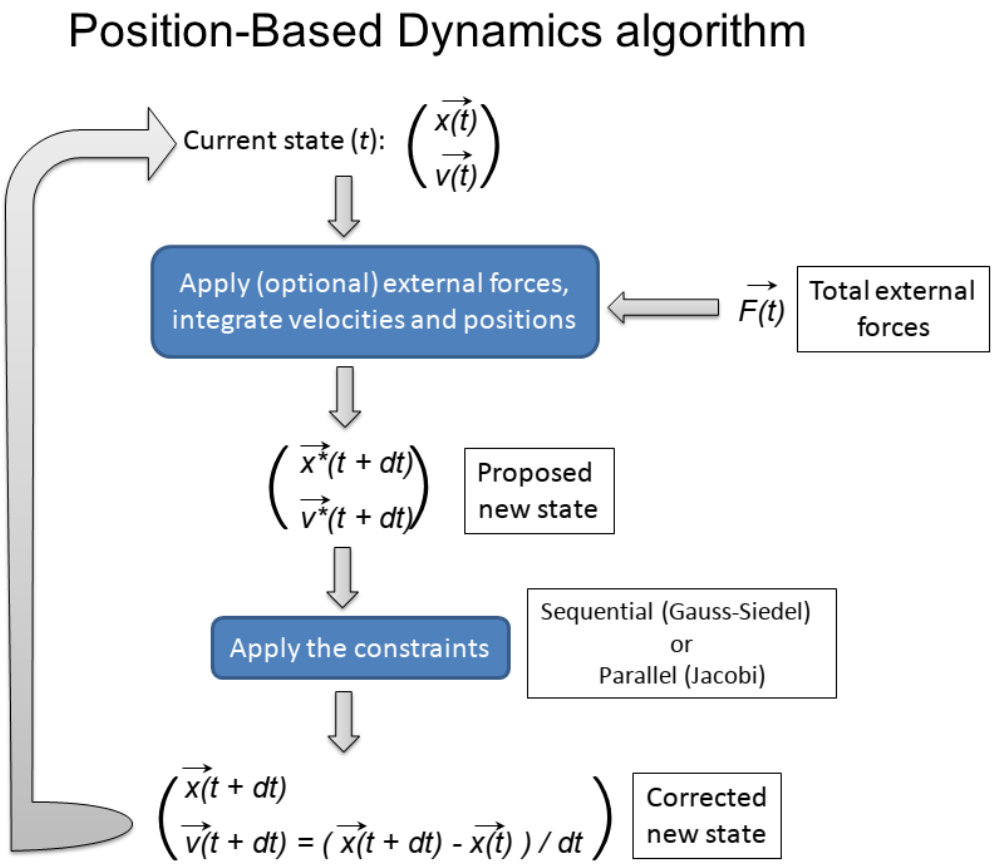

The generic algorithm for PBD is described as follow is pseudo-code:

```
// The algorithm assumes that each vertex in the model possesses the following
// attributes: velocity, position and mass.
// Vertices velocities are updated by applying the external forces (according to
// Newton's law) and it proposes new positions for each vertex.
for Vertex v in Vertices {
        v.previous_position = v.position;
        v.velocity += dt * (v.forces / v.mass);
        v.position += dt * v.velocity;
}

// The iterative solver applies the constraints to the proposed vertices
// positions, adjusting them such that they satisfy the constraints.
for i in iterations
        project_constraints(contraints, vertices);
```

```
// Finally, adjust vertices velocity based on the new adjusted positions
for Vertex v in Vertices
      v.velocity = (v.position - v.previous_position) / dt;
```

To provide a simple example of PBD constraint, consider the typical mass-spring system where two masses (usually represented by mesh vertices) are connected by an elastic spring. The elasticity of the spring applies a force on the masses which induces acceleration and velocity. In the PBD formulation, the same is achieved by the projecting the constraint $\boldsymbol{C(p_1, p_2) = |p_1 - p_2| - d}$; $\mathbf{p_1}$ and $\mathbf{p_2}$ are the vertices positions and $\boldsymbol{d}$ is the spring resting length. The resulting corrections $\Delta\mathbf{p_i}$ are subsequently weighted according to the inverse masses $\mathbf{w_i = 1/m_i}$. PBD has been implemented in the current model by adapting the code library available at https://github.com/InteractiveComputerGraphics/PositionBasedDynamics.
The current model implements distance, shape, strain, bending and pressure constraints (Figures S4A and S4B), according to the following rules:

1. The distance constraint controls the distance between connected vertices[97]. This constraint is useful to simulate elastic and plastic behavior. Cell edges can be either internal to the cell (representing the internal cytoskeleton and pectin matrix) or on the border (representing the cell walls). Edges have a different stiffness for extension and compression. Cells are generally regarded as incompressible objects so we assume maximum compression stiffness. Internal edges are meant to represent the cell pectin matrix and implemented as a viscoelastic material. Border edges represent the cell walls and are very stiff in order to prevent cell swelling from turgor pressure but can be relaxed through the action of auxin to allow cell growth.
2. The shape constraint[97] simulates the mechanical forces involved in the preservation of the cell structure. The shape constraint prevents cell deformation and collapse under external forces while allowing cell growth under internal pressure.
3. The strain constraint makes anisotropic growth possible[99]. This constraint is applied on mesh triangles restricting deformation according to cortical microtubules orientation. Disordered microtubules organization results in isotropic growth, while ordered microtubules produce anisotropic growth.
4. The pressure constraint[97] mimics cell osmotic pressure. This constraint is always active and allows cell expansion, which can be opposed by cell wall stiffness and restricted in a certain direction by the strain constraint (according to cortical microtubules organization). This constraint is different from previously discussed constraints because it also implements a special version of Position-Based Dynamics, called XPBD[100]. Simple PBD does not consider time in its original implementation, which makes it inadequate for growing constraints like pressure, since it does not replicate a physical realistic behavior. The pressure constraint has therefore been implemented in XPBD, making it more time-compliant.
5. The bending constraint prevents cell walls angle to drift too far away from the resting condition[97], hence avoiding cell collapse, mimicking cytoskeleton robustness.

Supplementary Table S1.

Model parameters description and value.

Parameter	Description	Value	Unit
Cell Polarization Model			
R_{MF}	CMTs reorientation rate	0.02	h^{-1}
d_{MF}	CMTs degradation rate	0.01	h^{-1}
Auxin transport Model			
K_{AUX1}	coefficient of auxin importing rate by AUX/LAX	1	µm/h
K_{PIN}	coefficient of auxin export rate by PIN	1.4	µm/h
$AUX1_b$	AUX1/LAX basal expression	1	h^{-1}
$AUX1_{expr}$	auxin-induced AUX1/LAX maximal expression	30	h^{-1}
$AUX1_{Max}$	maximum concentration of AUX1/LAX	2	$nM/\mu m^2$
$AUX1_K$	auxin-induced AUX1/LAX expression coefficient	0.01	$nM/\mu m^2$
d_{AUX1}	AUX1/LAX degradation rate	0.08	h^{-1}
PIN_b	PIN basal expression	0.2	h^{-1}
PIN_{expr}	auxin-induced PIN maximal expression	50	h^{-1}
PIN_K	auxin-induced PIN expression coefficient	0.05	$nM/\mu m^2$
PIN_{Max}	maximum PIN concentration inside the cell	2	$nM/\mu m^2$
d_{PIN}	PIN degradation rate	0.08	h^{-1}
D_{auxin}	Auxin diffusion rate in the intercellular space	1	µm/h
$AUX1_{tr}$	AUX1/LAX trafficking rate	1	h^{-1}
$AUX1_{MaxMem}$	maximum concentration of AUX1/LAX on membrane sections	15	μm^{-1}
PIN_{tr}	PIN trafficking rate	1	h^{-1}
PIN_{MaxMem}	maximum concentration of PIN on membrane sections	15	μm^{-1}
d_{PINmax}	maximum PIN degradation on the membranes	0.8	h^{-1}
P_{mem}	membrane permeability	0.2	µm/h
$d_{auxinBase}$	basal auxin degradation	0.0125	nM/h
$d_{auxinMax}$	maximum auxin degradation	0.125	nM/h
$K_{auxinMax}$	coefficient for half-max auxin degradation	5	$nM/\mu m^2$
kMF	coefficient of contribute of CMTs orientation to PIN sensitivity	0	1
kP	coefficient of contribute of auxin flow to PIN sensitivity	3	1
kMFP	coefficient of interaction CMTs orientation + auxin flow contributes to PIN sensitivity	3	1
Kmf	coefficient of half-max contribute of CMTs orientation to PIN sensitivity	0.5	1
Kgeom	coefficient of half-max contribute of cell geometry to PIN sensitivity	0.5	1
Auxin-flux and Auxin-concentration methods			
Kflux	coefficient of half-activation of PIN sensitivity contribution by auxin-flux	0.1	1
D_{reg}	regulator diffusion rate	1	h^{-1}
D_{pol}	polarizer diffusion rate	0.1	h^{-1}
$Kdisp_{POL}$	polarizer displacement rate	10	h^{-1}
$Kreg_{tr}$	regulator base trafficking rate	1	h^{-1}
$Kpol_{tr}$	Polarizer base trafficking rate	0.01	h^{-1}
$Kreg_{IAA}$	regulator half-max trafficking rate activation by auxin	0.01	$nM/\mu m^2$
$Kpol_{IAA}$	polarizer half-max trafficking rate activation by auxin	0.01	$nM/\mu m^2$
$Kreg_{GradT}$	regulator max trafficking rate activation by auxin gradient	1	$nM/\mu m^3$

$Kreg_{GradK}$	regulator half-max trafficking rate activation by auxin gradient	1	nM/μm^3
$dPOL$	regulator decay rate	0.08	h^{-1}
$dREG$	polarizer decay rate	0.08	h^{-1}
$Kpol_{IP}$	half-max activation of auxin flow contribution on PIN sensitivity by polarizer amount	0.1	1
Root Growth Model			
kE_{Max}	cell wall maximum stiffness	1	1
K_{1auxin}	auxin-induced cell wall relaxation coefficient	0.05	1
K_{2auxin}	auxin-induced cell wall stiffening coefficient	3	1

1486